

Article

A Novel MPPT-Based Lithium-Ion Battery Solar Charger for Operation under Fluctuating Irradiance Conditions

Khaled Osmani ¹, Ahmad Haddad ^{2,3}, Mohammad Alkhedher ⁴, Thierry Lemenand ¹, Bruno Castanier ¹
and Mohamad Ramadan ^{2,3,*}

- ¹ LARIS EA 7315, Polytech Angers, University of Angers, 49000 Angers, France; khaled.alosmani@etud.univ-angers.fr (K.O.); thierry.lemenand@univ-angers.fr (T.L.); bruno.castanier@univ-angers.fr (B.C.)
- ² School of Engineering, International University of Beirut BIU, Beirut P.O. Box 146404, Lebanon; ahmad.haddad@liu.edu.lb
- ³ School of Engineering, Lebanese International University LIU, Bekaa P.O. Box 1803, Lebanon
- ⁴ Mechanical and Industrial Engineering Department, Abu Dhabi University, Abu Dhabi P.O. Box 59911, United Arab Emirates
- * Correspondence: mohamad.ramadan@liu.edu.lb

Abstract: Fluctuant irradiance conditions constitute a challenge in front of a proper battery charging process, when originated from a PhotoVoltaic Array (PVA). The behavior of the PVA under such conditions (i.e., reflected by a disturbed PV characteristic curve) increases the complexity of the total available power's extraction process. This inconvenient fact yields eventually to a decreased overall efficiency of PV systems, especially with the presence of imprecise power-electronics involved circuits. Accordingly, the purpose of this paper is to design a complete battery solar charger, with Maximum Power Point Tracking ability, emerged from a PVA of 1.918 kW_p, arranged in Series-Parallel topology. The targeted battery is of Lithium-Ion (Li-I) type, with 24 VDC operating voltage and 150 Ah rated current. The design began by configuring an interleaved synchronous DC-DC converter to produce a desired voltage level, with low inductor ripple current and low output ripple voltage. The DC-DC converter is in turns condemned by a modified Perturb and Observe (P&O) algorithm, to ensure efficient maximum power tracking. Progressively, the design encountered a layout of the bi-directional DC-DC converter to ensure safe current charging values for the battery. Under the same manner, the role of the bi-directional converter was to plug the battery out of the system, in case when the Depth of Discharge (DoD) is below 25%, thus sustaining the life span of the battery. The entire setup of the proposed sub-systems then leads to the relatively fastest, safest, and most reliable battery charging process. Results show an effectiveness (in terms of PV power tracking) ranging from 87% to 100% under four swiftly changing irradiance conditions. Moreover, this paper suggested the design's future industrialization process, leading to an effective PV solar charger prototype.

Keywords: MPPT; DC-DC converter; perturb and observe algorithm; shading; irradiance; control



Citation: Osmani, K.; Haddad, A.; Alkhedher, M.; Lemenand, T.; Castanier, B.; Ramadan, M. A Novel MPPT-Based Lithium-Ion Battery Solar Charger for Operation under Fluctuating Irradiance Conditions. *Sustainability* **2023**, *15*, 9839. <https://doi.org/10.3390/su15129839>

Received: 11 April 2023

Revised: 12 June 2023

Accepted: 12 June 2023

Published: 20 June 2023



Copyright: © 2023 by the authors. Licensee MDPI, Basel, Switzerland. This article is an open access article distributed under the terms and conditions of the Creative Commons Attribution (CC BY) license (<https://creativecommons.org/licenses/by/4.0/>).

1. Introduction

The massive growth of PhotoVoltaic (PV) systems' installations is globally witnessed, where their utilization is evident across various applications [1–3]. Among different forms of renewable energy supplies, the PV systems are mainly popularized to be adapted as resilient electrical power provisions, due to their silent performance, static architecture, non-detrimental nature, and for the abundancy of solar irradiance [4,5]. The improved maintenance techniques for PV systems [6–19], and the amelioration of the PV cells' raw materials [20–27], have yielded in an elevated overall efficiency, hence approbated their approval to be considered as next-generation electrical power providers. For example, in order to remove the toxic air pollutants (CO₂, greenhouse gas emissions, etc.) resulting from

the excessive burning of oil, gas and diesel for energy generation purposes, PV systems can well contribute, heading relatively towards a carbonless future [28–36].

Having various forms and structural designs, off-grid PV systems are receiving the highest interest [37–41], as they present an elevated flexibility in front of low solar irradiance scenarios, as well as possessing the ability to supply loads during nights. In terms of reliability, off-grid PV systems can fit in commercial, industrial, and residential power systems [42,43], hence having a greater applicability in different fields of application. Nevertheless, such systems lower electricity bills and consist of a backup power supply for grid failures/blackouts by:

- Reducing the need for diesel and fuel to generate electricity
- Decreasing the urge for the continuous generators' maintenance and monitoring routines
- Making less technical labor routines

However, these systems rely mainly on Energy Storage Systems (ESS) [44–51]. The excess energy generated by the PV panels (i.e., during peak sunlight) is stored by a battery bank, for example. The continuous power supply demanded by critical loads can be hence ensured by the utilization of that stored energy. In terms of energy usage optimization, the ESS also contribute to load balancing and equity. Moreover, since grid outages/malfunction generally occur in electrical systems, the ESS feature in off-grid PV systems provide accordingly a backup supply, thus relatively smoothing out the fluctuations between the energy supply and demand. This reliance on ESS on the other hand, provokes consecutive problems, thus arising the need for:

- Maximum solar power extractor to benefit from the total available power
- Power conditioning units for a safe voltage/current equalization
- Monitoring systems to continuously check the charging states, battery's feeding voltage, charging current, etc.

Accordingly, DC-DC converters (i.e., solid-state switch-controlled electronic hardware that are used to either boost or buck the desired output voltage, according to the feeding input levels) are designed to be controlled by Maximum Power Point Tracking (MPPT) algorithms [52–57] to compensate the highly non-linear behavior of the PV cells [58–62], thus extracting the maximum available power from the PV arrays. Classified as isolated and non-isolated layouts [63–72], the overall efficiency of such converters and performance are related to their designs' complexity. For instance, non-isolated DC-DC converters showed better efficiency versus isolated ones, but still exhibit erroneous behaviors such as power loss and rippled currents. Generally, and according to the work conducted in [63–72], it can be concluded that isolated DC-DC converters offer higher efficiency when compared to non-isolated converters due to the reduced power losses, while ensuring galvanic isolation, thus offering an improved electrical safety (i.e., against ground loops, etc.). Due to their isolation barrier, isolated DC-DC converters exhibit low ripple current, hence reducing the electromagnetic interference noise. On the other hand, however, isolated DC-DC converters are more complex in their designs, with larger sizes and heavier weights due to the presence of the isolation transformers. From another side, and after an investigation of the work in [63–72], it can be deducted that non-isolated DC-DC converters require fewer components for their realization and are more suitable for space-constrained applications when compared to isolated converters. Despite these advantages, the non-isolated DC-DC converters are less efficient when compared to the isolated converters and are prone to exhibit high-frequency harmonic oscillations. With that being said, the choice of a DC-DC converter for off-grid PV systems is a challenging task, which needs consideration according to many operational factors.

The MPPT algorithms on the other hand (i.e., composing the software which produces case-dedicated duty values, that in turn control the behavior of the solid-state switches in the DC-DC converters), are characterized for operation under uniform irradiance [73–82] or under partial shading conditions [83–99]. Such algorithms fluctuate in their complexity

levels and accuracy, ranging from simple (i.e., Perturb and Observe (P&O)) to complex (i.e., artificial-intelligence-based algorithms). The relation between the MPPT algorithm's complexity and its level of accuracy is reversal, where the simpler the algorithm is, the worse its efficiency becomes when compared with higher-level algorithms. As for the MPPT algorithm used under homogeneous irradiance conditions in [73–82], they can be perceived as simple in application, have low computational requirements, and possess a fast response criterion. On the opposite side, such algorithms perform poorly under partial shading conditions, where they may exhibit an oscillatory behavior around the maximum power point, leading thus to a “false” peak in the PV's characteristic curve, and are generally vulnerable to local power maximum traps. On the other hand, the other MPPT algorithms that are used under partial shading conditions in [83–99], have a better improved efficiency than the ones in [73–82], where they can accurately identify the global power peak under complex and non-linear shading conditions. Still, such algorithms are way more complex to implement, where the artificial-intelligence-based [86] need training with a representative dataset, thus relying on accurate models and training data. Accordingly, and as it is the case with the choice of the DC-DC converters, the choice of the MPPT algorithm to be implemented in a PV-based solar charger, is also not a straightforward approach.

Charge controllers from another side, regulate the power flow from/into the ESS, by means of DC-DC converters (e.g., bi-directional, uni-directional, etc.) [100–103]. Such converters can be controlled using a Proportional Gain (PG) controller, reference voltage/current control scheme, closed-loop control, and others [104,105]. The uni-directional charge controllers in [100–103] have a simple design and are generally more cost-effective than the bi-directional converters, and offer a standard protection for the PV panels, since they allow the power flow in one direction (i.e., the route from the ESS to the PV panels is opened, hence the panels would never be subjected to any current from the ESS). On the other hand, uni-directional charge controllers have more limited functionality when compared to bi-directional converters, where they do not support the power flow from multiple PV sources. The bi-directional charge controllers, on the other hand, are more flexible in usage, enable more energy management than uni-directional controllers, and better facilitate the grid-integration with the PV systems. Despite their advantages, the bi-directional charge controllers are more complex in design, thus yielding to a reduced cost efficiency when compared to the uni-directional controllers and require advanced algorithms to ensure a stable operation. The controlling scheme in [104,105] is by itself another area of study, where for example the PG controller offers a good stability with appropriately tuned gains but can unfortunately show poor performance such as presence of overshoot, instability, current leakage, and others, [106] under improper gain tuning. Under the same approach of the DC-DC converter choice, as well as the MPPT algorithm, the charge controllers, on the other hand, require a careful selection process, when intended to be employed in off-grid PV systems.

Based on what has been precedent, and by taking into consideration the challenges for choosing a DC-DC converter to be controlled by an appropriate MPPT algorithm which dictates the operation of the charge controller, the aim of this paper is to design a novel solar battery charger, beginning by the design of an interleaved synchronous non-isolated DC-DC converter. According to the surveyed DC-DC converters, and after analysis of the pros and cons of each, in order to mitigate ripple current and minimize the equipment need and size of the converter, the interleaved synchronous non-isolated converter is chosen. The modification of the P&O algorithm presented in this work rearranged the proportionality between the algorithm's complexity and accuracy level, where a simple algorithm (far from artificial intelligence and machine-language-based methods) showed better accuracy than conventional P&O, and hence offered an intermediate trade-off.

- The bi-directional DC-DC converter used to control the charging/discharging processes of the battery is designed and controlled via PV array specifications (voltage, current, power, etc.)-based algorithm. At the final destination, the reference current (I_{ref}) is developed and interfered with a Proportional Integral (PI) controller to safely

charge the 24 V, 150 Ah Lithium-Ion (Li-I) battery with the maximum available current, resulting from different shading patterns. Accordingly, this paper's contribution can be summed up in the following points: improved design of a DC-DC converter: interleaved synchronous non-isolated converter, providing good efficiency, at the same time presenting low ripple currents.

- Modified MPPT algorithm: simply by adding an operational timer on the workflow process of a conventional P&O algorithm, the "real" power peak is more precisely identified, hence achieving a more power extractability option from the PVA.
- Enhanced bi-directional charge controller: not only does it ensures maximum safe charging current values for the ESS, but also plugs the battery out of the system according to a threshold SoC, yielding eventually in prolonging its lifecycle (when applied as a prototype).

The overall systematic design is a combination of multiple sub-systems, beginning with the PV Array (PVA) that is arranged in a 3×3 Series Parallel (SP) topology, with a maximum power of 1.918 kWp. The designed PVA is then succeeded with an interleaved DC-DC converter (controlled by modified P&O algorithm) which in turn is interfered with a bi-directional DC-DC converter (controlled by a reference current generator). The output target is to maximally charge the Li-I battery in the safest, fastest, and most accurate form.

The rest of this paper is composed as follows: Section 2 presents the overall working methodology behind the work in this paper, Section 3 reveals the PVA arrangement and different shading patterns used during the Matlab simulation of this design, Section 4 shows the designing steps for the interleaved DC-DC converter, Section 5 explains how the P&O was modified. Section 6 interprets the design structure of the bi-directional converter, which is controlled by current suppression scheme shown in Section 7, where in Section 8 the entire design, grouping physical structures (converters) with control and measurement modules (algorithm, scoping, etc.) is shown, and being subjected to four distinct irradiation patterns, Section 9 discusses the obtained results and offers future work plans for the design, and finally in Section 10 global conclusions are derived.

2. Working Methodology

In order to completely realize the work suggested in this paper, that is to design a complete solar charger, originated from the PVA, the design of each sub-component (e.g., DC-DC converter, bi-directional converter, etc.) is thoroughly investigated. Each of the electronic components are designed according to a mathematical model, yielding for the calculation of the required elements, such as resistors, capacitors, inductors, and others. The modification of the P&O algorithm, on the other hand, was based on a computational assessment in which the conventional P&O cannot dedicate accurate duty ratios in order to maximally extract the available power from the PVA under different shading scenarios. The working methodology behind this work can be summarized according to the following points:

1. While attempting to mimic some extremely fluctuating solar irradiance conditions, the designed solar irradiance patterns in the Simulink environment varied from 100 W/m^2 to 1000 W/m^2 with different time lapses. For example, one of the solar irradiance patterns can have its irradiance step-wise of 100 W/m^2 decreased from 1000 W/m^2 to 100 W/m^2 during non-static time frames: a condition of 1000 W/m^2 irradiance can last, for example, x seconds, then 900 W/m^2 for y seconds and so on, until the minimum of 100 W/m^2 for example is reached. Different irradiance cycles exist for each of the designed irradiance patterns. This shall serve to emulate extreme solar irradiance fluctuating conditions (i.e., in real applications, such scenarios will be due to extreme cloud passage, swiftly moving physical obstacles, etc.)
2. According to the surveyed DC-DC converters from the work in the references [63–72], the mathematical model of the suggested interleaved synchronous DC-DC converter is justified after responding to the following questions:
 - a. Based on what must the converter's switching frequency be?
 - b. How to calculate the duty ratio?

- c. What are the values of the capacitance/inductance for the converter's capacitor/inductor, respectively?
3. Concerning the MPPT algorithm (i.e., P&O) modification, and in order to stay away from further programming complexities, the work in this paper simply suggests analyzing the PV power curve using discretized samples by means of a code-based on-delay timer. The modified P&O can hence better "acknowledge" the power status of the PVA, thus more accurately assign duty ratios.
4. For an efficient implementation of the suggested bi-directional converter, its electrical parameters must be also modelled mathematically, for an optimum selectivity of inductance, capacitance, and resistance that are to be employed in its circuit architecture. Moreover, the bi-directional converter must take also into consideration the maximum allowed charging current, as well as the minimum permissible depth of discharge.

By taking all of the previous steps into consideration, a complete version of the solar charger is hence produced, in a cascaded topology, beginning by the PVA as main input, then successively toward the DC-DC converter (controlled by the modified P&O algorithm), then the bi-directional converter (controlled by a current control scheme), then eventually to the battery's terminals.

3. Set Up of PVA and Creation of Irradiation Patterns

The PVA with the power rating of 1.918 kWp, consisting of the input of this design, is sub-composed of multiple PV modules, each of a smaller power rating. Using the Series-Parallel (SP) interconnection scheme, the PVA is accordingly built. This type of PV Reconfiguration (PVR) is adapted among many others, such as parallel, series, Total Cross Tied (TCT), Honey Comb (HC), skyscraper puzzle, Sudoku, etc. [107–116] due to its superiority in terms of elevated efficiency and less need of extra interconnecting wires. The SP scheme is hence found optimum and would present an advantageous point for the future industrialization of the design, in regards to the system's cost efficiency. The electrical characteristics for each PV module composing the PVA are shown in Table 1. According to the parameters shown in Table 1, the PVA characteristic curves, such as Current-Voltage (I-V) and Power-Voltage (P-V) are plotted in Figure 1.

Table 1. Electrical characteristics of each PV module.

Module Data	Value	Model Parameters	Value
Maximum power	213.15 [W]	Light generated current	7.8654 [A]
Open circuit voltage	36.3 [V]	Diode saturation current	2.9273×10^{-10} [A]
Short circuit current	7.84 [A]	Diode ideality factor	0.98119
Voltage at maximum power V_{mpp}	29 [V]	Shunt resistance	313.0553 [Ω]
Current at maximum power I_{mpp}	7.35 [A]	Series resistance	0.39381 [Ω]

It can be noticed from Figure 1 that the maximum power affordable by the PVA at the Standard Test Conditions (STC) under an irradiance of 1000 W/m^2 and temperature of $25 \text{ }^\circ\text{C}$ is 1.918 kWp. The PVA, however, can encounter different shading scenarios, inhibiting it thus from achieving its maximum power capacity. This is mainly due to non-static shadow reflectors, such as moving clouds, birds, and other obstacles as shown in Figure 2.

In order to study the negative impacts of the probable rapidly fluctuating irradiance inducers as in Figure 2, a time-based irradiance signal generator is derived in this work, within a time frame of 10 s. The sensitivity of irradiance is set for 100 W/m^2 with a maximum time lapse of 1 s, as shown in Table 2, for different Solar Irradiation Patterns (SIPs). The logic behind the four shading patterns creation in Table 2 is derived after several assumptions, stating that at a defined time t , the incident irradiation hitting the PVA surface

is of a constant value x , resulting from clouds/birds' passage. For each irradiance value from 100 W/m^2 to 1000 W/m^2 , as well as for each SIP, indicated is the time of irradiance-subjection. For example, in Table 2, the SIP2 has no time window during which the PVA is subjected to an irradiance of 100 W/m^2 where this same condition also applies for SIP3. For SIP4 from another side, the PVA is subjected to an irradiance of 1000 W/m^2 , for example, only at $t = 5 \text{ s}$ and $t = 10 \text{ s}$. This corresponds to the logic for all SIPs in Table 2. According to the values driven in Table 2, the graphical representation for different shading patterns, SIP1, SIP2, SIP3, and SIP4 is presented in Figure 3.

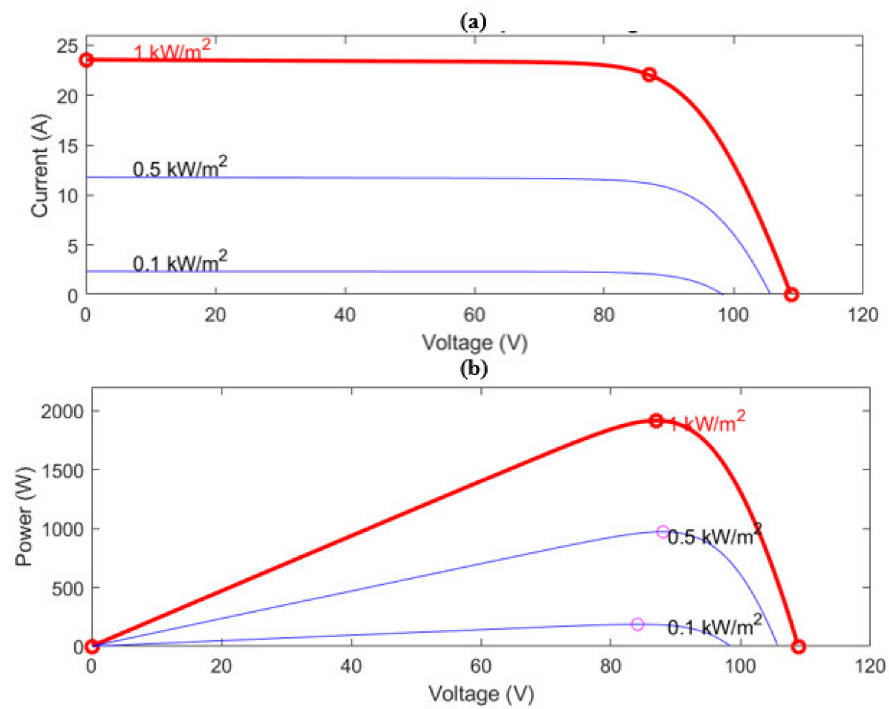


Figure 1. Characteristic curves for the SP PV array, (a) I–V curve, (b) P–V curve.

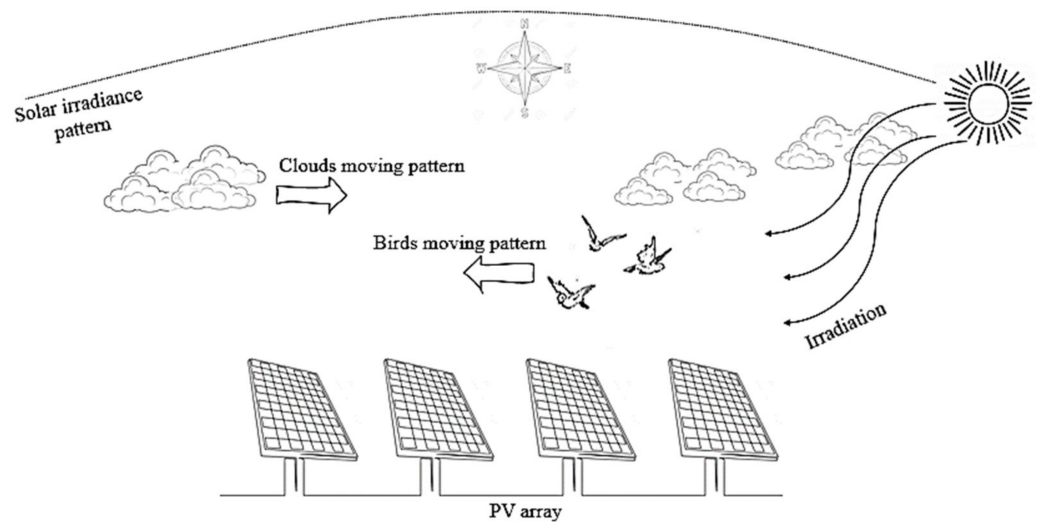


Figure 2. Causes of timely fluctuating shading scenarios.

Table 2. The data used for the irradiance curves generation.

Irradiance [W/m ²]	1000	t = 0 s t = 6.5 s	t = 1 s t = 2 s t = 4 s t = 7.7 s	t = 2 s t = 7.2 s t = 9 s	t = 5 s t = 10 s
	900	t = 0.7 s t = 2.7 s t = 6 s t = 8.2 s	t = 0.7 s t = 2.7 s t = 3.7 s t = 8 s	t = 1.7 s t = 2.2 s t = 7.2 s	t = 9 s
	800	t = 2 s t = 5 s t = 8.2 s t = 10 s	t = 1 s t = 2 s t = 6 s t = 8 s	t = 1.5 s t = 2.4 s t = 7 s t = 9.4 s	t = 8 s
	700	t = 1 s t = 2 s t = 3 s t = 7 s	t = 0.5 s t = 2.7 s t = 3.4 s t = 8.7 s	t = 1.2 s t = 2.7 s t = 5.2 s t = 6.7 s	t = 3 s
	600	t = 1.2 s t = 4.4 s t = 9.4 s	t = 1.2 s t = 5.4 s t = 8.4 s t = 9.4 s	t = 1 s t = 1.2 s t = 3 s t = 5 s t = 9.7 s	t = 1 s
	500	t = 1 s t = 3 s t = 5 s t = 7 s t = 8.7 s	t = 0 s t = 3 s t = 4.2 s t = 5.2 s	t = 0.75 s t = 1 s t = 3.26 s t = 3.49 s t = 4.74 s t = 0.5 s	t = 0 s
	400	t = 3.7 s t = 4.4 s t = 9.4 s	t = 8.7 s t = 9.4 s	t = 0.75 s t = 3.49 s t = 3.73 s t = 4.46 s t = 0.29 s	t = 2 s
	300	t = 3.6 s t = 9 s	t = 9 s t = 5.21 s	t = 0.5 s t = 3.73 s t = 4 s t = 0 s	t = 4 s
	200	t = 4.3 s t = 5.4 s	-	t = 0.29 s t = 4 s t = 4.24 s	t = 6 s
	100	t = 4 s t = 9 s	-	-	t = 7 s
Solar Irradiation Patterns	SIP1	SIP2	SIP3	SIP4	

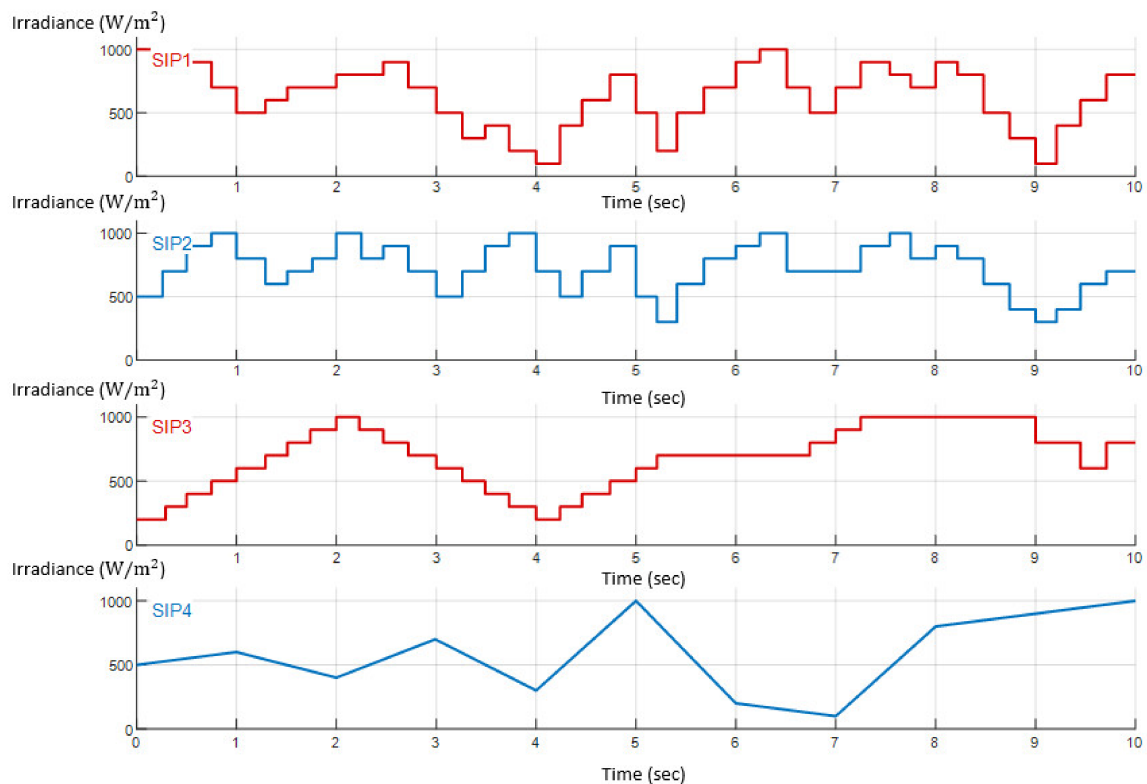


Figure 3. The four rapidly fluctuating distinct irradiation patterns.

4. Design of the DC-DC Converter

As intended to pull down the PVA output voltage, near the ESS voltage whilst maintaining the conservation of input/output power equalities, an interleaved synchronous buck converter is adapted in this work. First and foremost, the synchronous circuit form for the converter is an improved modification referring to the conventional buck converter [117]: the replacement of the diode with another solid-state switch (e.g., Metal Oxide Semi-conductor Field Effect Transistor (MOSFET), Insulated Gate Bipolar Transistor (IGBT), etc.) will negate any voltage drops across the diode, hence lowering losses and elevating the converter's efficiency. The synchronous buck converter is shown in Figure 4.

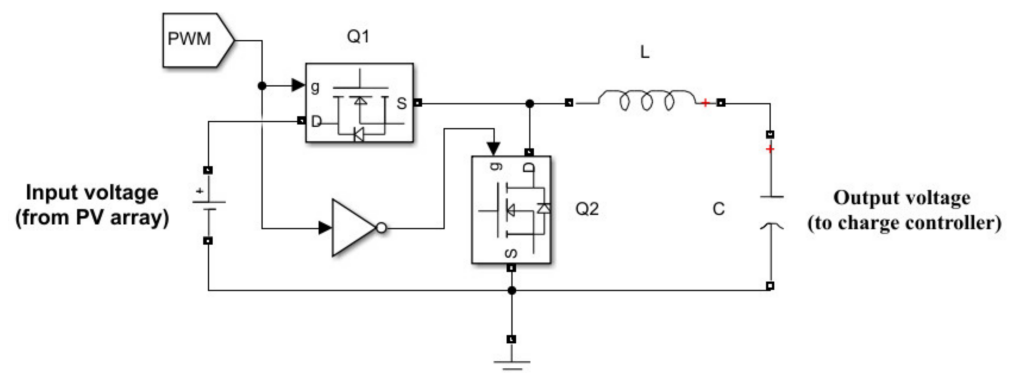


Figure 4. Synchronous DC-DC buck converter.

The Pulse Width Modulation (PWM) label shown in Figure 4 is obtained from the MPPT algorithm. The logic “NOT” gate, which is used in generating the gate signal to Q2, is there to ensure that both Q1 and Q2 are never conducting at the same time, thus eliminating any possibility of a bolted electrical short-circuit. Concerning its working routines, the circuit in Figure 4 operates under two modes:

1. Q1 is closed, Q2 is open: in this phase, the current flows in a clockwise direction, charging both inductor L and capacitor C .
2. Q1 is open, Q2 is closed: the energy stored in L is released, where current flows from the inductor itself. Under a certain threshold of inductor discharging, the capacitor becomes the main source of the current, until the next cycle begins.

The interleaved design used in this work takes two circuits of Figure 4 and connects them in parallel. The input and output capacitors are shared for the doubled circuit, as shown in Figure 5. The ripple current for the interleaved circuit is halved since each interleaved phase shares the total current.

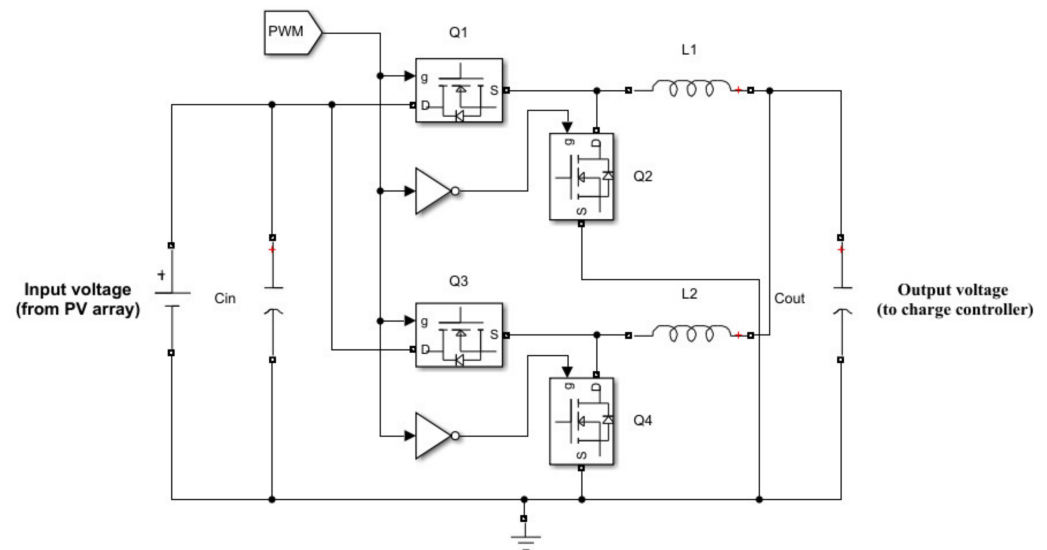


Figure 5. Interleaved Synchronous DC-DC buck converter.

The DC-DC converter circuit topology is to be based on an interleaved synchronous design, presenting an increased power handling capability (current and power are divided between the multiple converter phases). From the same perspective, the interleaved design provides also presents an improved efficiency by reducing the solid-state switches conduction losses (by distributing the load across multiple phases), as well as adapting a better transient response (the presence of multiple phases in the circuit architecture allows a better load sharing). The following parameters must be calculated in order to complete the design:

- Switching frequency f_s
- Duty ratio D
- Inductance L
- Capacitance C

The choice of f_s , for it to be followed by the PWM generation is solely based on the switching losses of the MOSFETs, where a higher f_s yields to smaller inductor and capacitor sizes, but in turn increases the switching losses as shown in Equations (1)–(3) for the high side MOSFETs [118–120].

$$P_{\text{Loss[H]}} = P_{\text{Conduction[H]}} + P_{\text{Switching[H]}} \quad (1)$$

$$P_{\text{Conduction[H]}} = I_{\text{OUT}}^2 \times R_{\text{DS}} \times D \quad (2)$$

$$P_{\text{Switching[H]}} = \left(\frac{t_{\text{RH}} + t_{\text{FH}}}{2} \right) \times V_{\text{in}} \times I_{\text{OUT}} \times f_s \quad (3)$$

Such that $P_{Loss[H]}$ denotes the total power losses on the high side MOSFETs, as a sum of conduction losses $P_{Conduction[H]}$ and switching losses $P_{Switching[H]}$. The term D represents the duty ratio generated by the MPPT algorithm, t_{RH} , t_{FH} the turn on/off (rise/fall) times, respectively, R_{DS} the drain to source MOSFET's resistance, V_{in} the input voltage to the converter originated from the PVA, I_{OUT} the output current, and f_s the switching frequency. Similarly, for the low side MOSFETs, the switching frequency related power losses are shown in Equations (4)–(6) [118–120].

$$P_{Loss[L]} = P_{Conduction[L]} + P_{Switching[L]} \quad (4)$$

$$P_{Conduction[L]} = I_{OUT}^2 \times R_{DS} \times (1 - D) \quad (5)$$

$$P_{Switching[L]} = \left(\frac{t_{RL} + t_{FL}}{2} \right) \times V_{bodyDiode} \times I_{OUT} \times f_s \quad (6)$$

where $V_{bodyDiode}$ represents the internal body diode forward drop voltage. As seen from Equations (1)–(6) the switching frequency is directly proportional to the MOSFETs' switching losses. Accordingly, a trade-off between L , C sizes and elevated losses, yields to an f_s choice of 15 kHz, for this design. The duty ratio D on the other hand, presented in Equation (7) must take into consideration that the output voltage is always equal to 26 V, as an effective and a safe feeding voltage level to the ESS of 24 VDC operating voltage.

$$D = \frac{V_{out} \times \text{eff}}{V_{in}} \quad (7)$$

where V_{out} , V_{in} represent the required output voltage and PV input voltage, respectively, with eff representing the converter's efficiency. Assuming a 100% efficiency (for simulation purposes only), and a V_{in} of 87 V (according to Figure 1), the duty ratio must be for instance equal to 0.298. This value is continuously increased/decreased according to the MPPT algorithm variations. Both L and C values can be calculated according to Equations (8) and (9) [121,122].

$$L = \frac{V_{out} \times (V_{in} - V_{out})}{\Delta I_L \times f_s \times V_{in}} \quad (8)$$

$$C = \frac{\Delta I_L}{8 \times f_s \times \Delta V_{out}} \quad (9)$$

Such that ΔV_{out} represents the ripple voltage, and ΔI_L the inductor ripple current expressed in Equation (10) [122].

$$\Delta I_L = (20\% \text{ to } 40\%) \times I_{out(max)} \quad (10)$$

According to Equations (7)–(10), and by taking into consideration the chosen value of f_s with a desired ripple voltage of 10 mV, the required parameters for the converter design are shown in Table 3.

Table 3. DC-DC converter parameters values.

Parameter	Value
f_s	15 kHz
D	29.8%
L	14.97×10^{-4} H
C	2.3641×10^{-4} F

5. Configuration of the MPPT Algorithm

A conventional P&O algorithm could lead to an erroneous behavior under swiftly varying irradiance conditions [117]. Specifically, for the shading patterns created in Figure 3, the shading intensity varies within a 0.1 s to 0.5 s time lapses. Accordingly, the power difference between ideal and actual power curves (dP), as well as the voltage difference between PV and input voltage curves (dV), could possibly lead to a “false” zero as shown in Figure 6. Therefore, an inaccurate duty ratio D is generated by the MPPT algorithm, provoking a decrease in the system’s efficiency, since the total available power from the PVA cannot be then extracted. The small valued power differences in the time frame (4s; 6s) for example, are not taken into consideration in the conventional P&O algorithm.

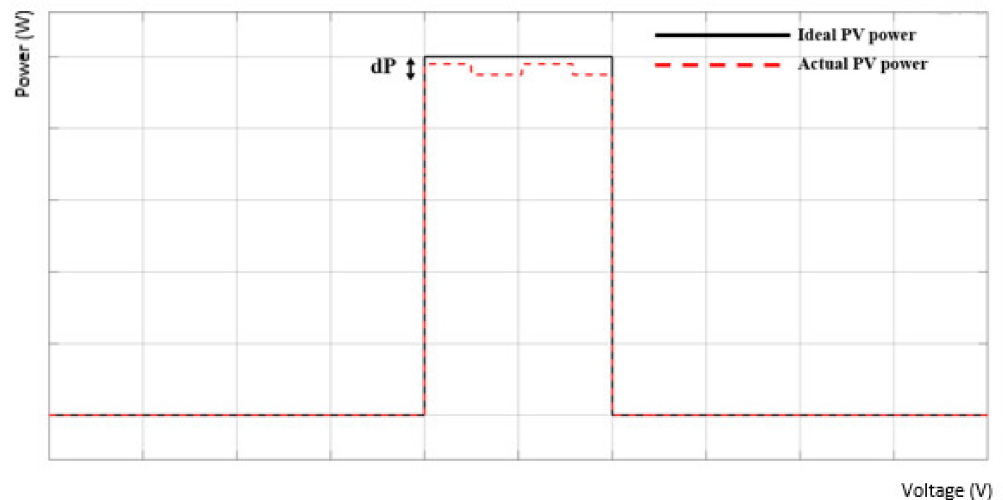


Figure 6. Misleading power differences in a conventional P&O algorithm.

The modification of P&O algorithm intended in this design is to achieve a “true” zero difference between dP quantities, hence attending a real maximum within the P-V characteristic curve. This process is achieved by setting a timer during the flow of the MPPT algorithm, which estimates the power differences using discrete samples and returning averaged values of dP to be investigated. Below are the process’ steps:

1. Continuously check whether dP is equal or not to zero, by establishing a timer at each time interval: if the sampled values of dP within the interval have a mean value of zero, then the entire power difference is equal to zero in that timing frame as shown in Figure 7.
2. Set the above sampling method at each new time interval.
3. All mean values resulting from all intervals must be equal to zero.
4. If the condition in the previous step is not satisfied, then modify the duty ratio respectively.

This sampling method could decrease the performance efficiency of the algorithm by requiring more time for execution. This in turn can be compensated by a conditional statement at each checkpoint of dP . According to the I-V and P-V curves shown in Figure 1, the power difference can be checked after the voltage is equal to 80 V, since the maximum peak lies to its right. The complete modified P&O flowchart is expanded in Figure 8.

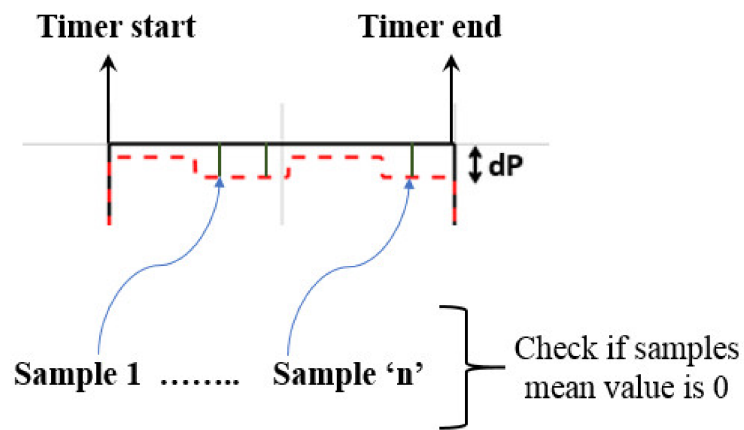


Figure 7. Sampling of power differences in a time frame.

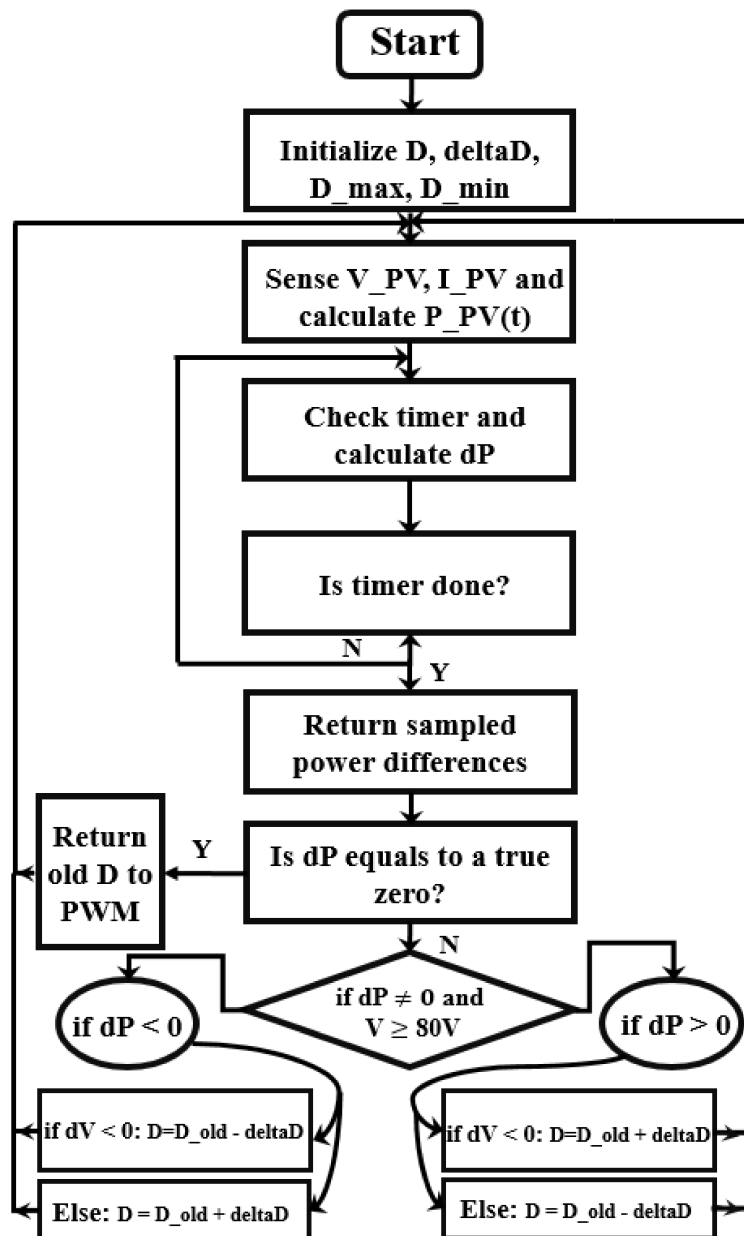


Figure 8. Modified P&O flowchart.

6. Modeling of the Bi-Directional Converter

So far, the design comprising the DC-DC converter, accompanied by the modified MPPT algorithm, offers a maximum power extraction from the PVA under different fluctuating SIPs. Regardless of the solar irradiance's intensity, the modified P&O algorithm ensures accurate as well as dynamic duty ratios generations in order to equivalently set the action of the DC-DC converter (i.e., the conducting/non-conducting states of the solid-state switches). However, it still cannot be confronted with the ESS, due to the following reasons:

- Inability to maintain safe current charging levels for the ESS under high irradiance conditions. The charging current delivered by the PVA might exceed the nominal current charging rate, related to the ESS as indicated in Table 4.
- When the charging currents are not balanced, the ESS gets overcharged, hence, its lifecycle would be reduced consecutively.
- Under discharging states (i.e., at nights or during low irradiance conditions) the battery can exceed the recommended Depth of Discharge (DoD), also causing an increase in its aging rate, and quicker deterioration.

Table 4. Characteristics of the Li-I battery.

Battery Parameter	Value
Rated voltage	24 V
Rated capacity	150 Ah
Cut-off voltage	18 V
Fully charged voltage	27.9357 V
Nominal charging current	58 A

According to Table 4, when the charging current provided by the PVA exceeds 58 A, the battery's internal electrodes become flooded, thus risking deterioration and posing hazards to the surrounding environment (i.e., risk of burnouts, explosions, etc.). Consequently, the designed bi-directional DC-DC converter offers current charging safety for the battery, with respect to the data in Table 4. From a first point of view, the battery's charging current should never exceed 58 A, where the DoD must never be below 25%. This converter is designed using two MOSFET switches, one for the charging process, the other for the discharge, with an LC circuit, where a dummy resistive load is added to interpret the DoD, as shown in Figure 9. Additionally, a controlled switch to plug in/out the battery in case of with respect to DoD is added.

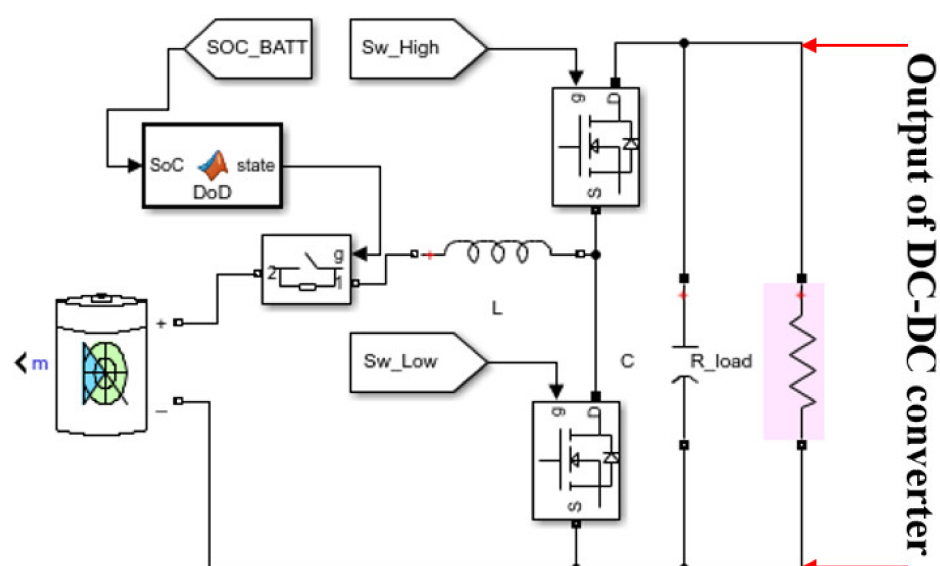


Figure 9. The bi-directional DC-DC converter design.

Regardless of the tactic used to control the circuit in Figure 9, which will be presented in-depth in Section 7, the inductor L and the capacitor C are selected based on Equations (11)–(12), respectively [123].

$$L = \frac{D \times (V_{\text{int_synch_conv}} - V_{\text{batt_charge}})}{f_S \times \Delta I_L} \quad (11)$$

$$C = \frac{(1 - D) \times V_{\text{batt_charge}}}{f_S^2 \times 8 \times L \times \Delta V_{\text{out}}} \quad (12)$$

Such that D represents the duty ratio of PWM generation for the MOSFETs, f_S the switching frequency, ΔI_L the desired inductor ripple current, $V_{\text{int_synch_conv}}$ the actual voltage outputted from the interleaved synchronous DC-DC converter designed in Section 3, $V_{\text{batt_charge}}$ the needed voltage level to feed the battery. On the other hand, ΔV_{out} denotes the output ripple voltage. Subsequently, the items composing this bi-directional converter are revealed in Table 5.

Table 5. Parametric values for the bi-directional converter design.

Item	Value
L	2.5 mH
C	3300 μF
R	200 Ω

7. Current Suppression and DoD Control Schemes

The circuit of Figure 9 possesses two switches controlled via PWM generation. The rule is to always keep the two switches phase sequenced as both should never be mutually on or off, as indicated in Figure 10. The high side MOSFET conducts as long as there is sufficient power to charge the battery (i.e., presence of solar irradiance). The inductor L in Figure 9 acts as a current suppressor, while continuously changing its impedance, according to the different PWM states, with respect to Equation (13).

$$Z = \sqrt{R^2 + X_L^2} \quad (13)$$

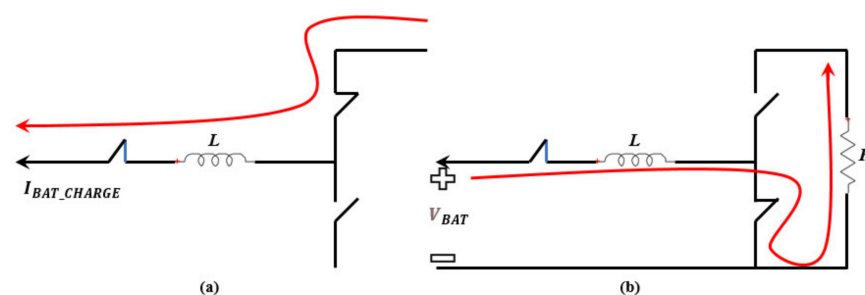


Figure 10. Power flow in/out the battery, (a) charging case (b) discharging case.

With Z denoting the impedance of the inductor, R its Equivalent Series Resistance (ESR) and X_L its reactive inductance. Assuming a perfect inductor (i.e., $\text{ESR} = 0$), the current passing through is shown in Equation (14).

$$I_L = \frac{V_L}{X_L} = \frac{V_L}{2\pi f L} \quad (14)$$

With V_L representing the voltage across the inductor, f the switching frequency and L the inductance. Accordingly, the continuous change of X_L with respect to f acts as a current limiter, while extracting its maximum safe quantity.

The battery charging current I_{BAT_CHARGE} must never exceed 58 A as a maximum value according to Table 4. For instance, at 1000 W/m^2 the maximum value of the current that is extractable from the PVA is valued at 58 A, where at 500 W/m^2 , its value becomes 33 A. With that being said, a reference current I_{ref} , which is mainly dependent on the solar irradiance levels, must be considered as a reference for high/low sides MOSFETs PWM generation. To ensure that I_{BAT_CHARGE} is as closest as possible to I_{ref} , these two quantities are differentiated, where the resulting error signal (if any) will later be fed into a Proportional Integral (PI) controller as shown in Figure 11.

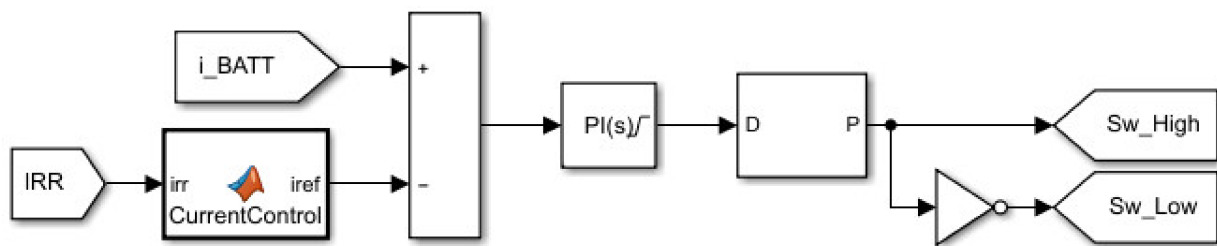


Figure 11. Battery charging current control.

The PWM signals for the MOSFETs in Figure 9 are hence directly controlled by the PI output, with the latent aiming to have the lowest error between I_{BAT_CHARGE} and I_{ref} . On the other hand, in order to monitor the DoD and make sure that the battery would be automatically plugged out of the entire circuit when $DoD \leq 25\%$, a controlled switch is added, as seen in Figure 9 that works as follows:

- As long as $DoD > 25\%$, a high logic is set on its gate signal, hence forcing it to be closed (i.e., in a conduction state)
- The above process workflow is halted when the DoD that is acknowledged from battery SoC, drops below 25%.

Both current suppression and DoD control schemes will eventually charge the battery with maximum safe current level, while not permitting the battery to discharge below 25% under low irradiance scenarios and during nights.

8. Overall Layout with Results

The overall circuit, which is composed of multiple designs investigated from Section 2 to Section 6, is shown in Figure 12. In this circuit, the SIPs are to be manually chosen, from the irradiance signal builder. For each SIP, exist different simulation results in terms of the battery charging current, SoC, the feeding voltage, and the overall efficiency. The PVA is set under 25°C for all SIPs, having its ideal voltage and current referred to as V_{PV} and I_{PV} , respectively, where V_{IN} represents its actual output voltage. The entire circuit of Figure 12 is subsequently arranged with respect to each of its sub-components: the signal builder with the PVA representing the input, to the DC-DC converter, the bi-directional converter, all the way along the battery's terminals. As for the control schemes, the MPPT algorithm is written within a Matlab script, having V_{PV} , I_{PV} , V_{IN} , and P_{IDEAL} as inputs, such that after the modified P&O flowchart execution, a "duty" is outputted, where it controls the solid-state switches of the interleaved DC-DC converter. The bi-directional converter, on the other hand, is operated with the current control scheme, by means of the final output of the PI controller.

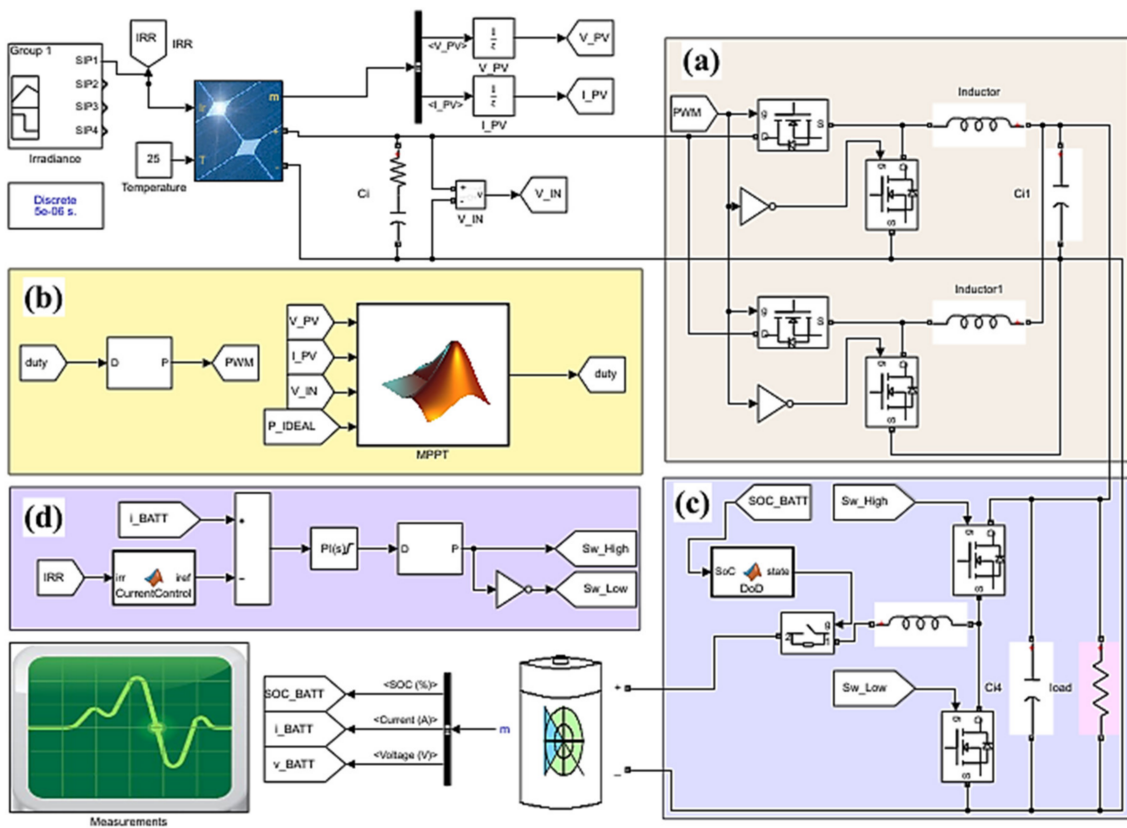


Figure 12. The solar charger overall design, (a) interleaved synchronous DC-DC converter, (b) MPPT algorithm, (c) bi-directional DC-DC converter, (d) current suppression and DoD control schemes.

The “Measurements” subsystem block, included in Figure 12, involves scopes circuitry, mean efficiency calculations, and power conversion as revealed in Figure 13: for example, the P_{PV} is calculated based on a scalar multiplication of I_{PV} and V_{PV} . The efficiency is scoped from another part, based on the numerical assessment between P_{IDEAL} and P_{PV} . For each of the SIPs, the measurements subsystem block of Figure 13 outputs different graphs covering the alignment between the P_{IDEAL} as well as P_{PV} and other battery related electrical characteristics/processes.

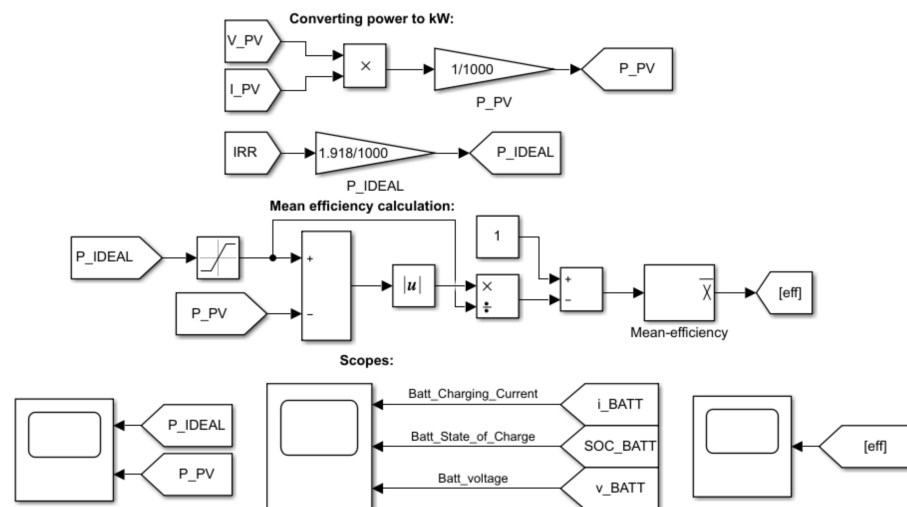


Figure 13. Measurements block subsystem.

8.1. Results for SIP1

The design shown in Figure 12 will be successively exposed to all different irradiance patterns. For this case, the application of SIP1 as designed in Figure 3 would reflect the response of the entire circuit, by showing the closeness between the actual and the ideal power curves as shown in Figure 14. On the other hand, the battery charging process, including the charging current, state of charge, and battery voltage are shown in Figure 15. Lastly, Figure 16 reveals the mean efficiency for the design. The analysis of these results for all SIPs is to be investigated in Section 8.

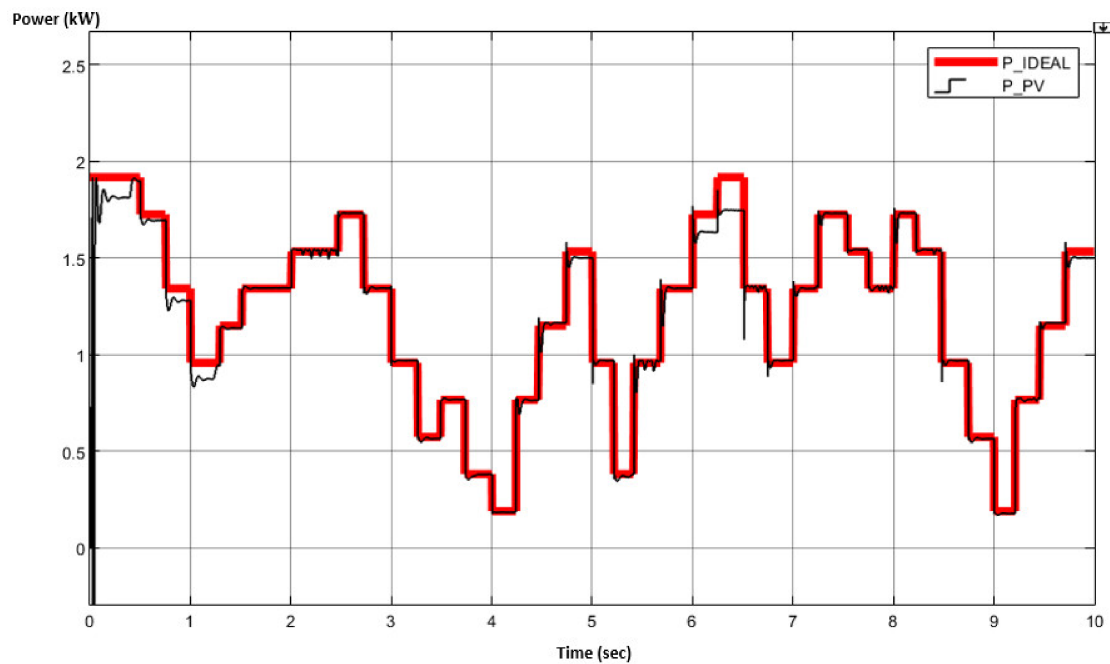


Figure 14. The alignment between the ideal and actual PV power curves (kWp) for SIP1.

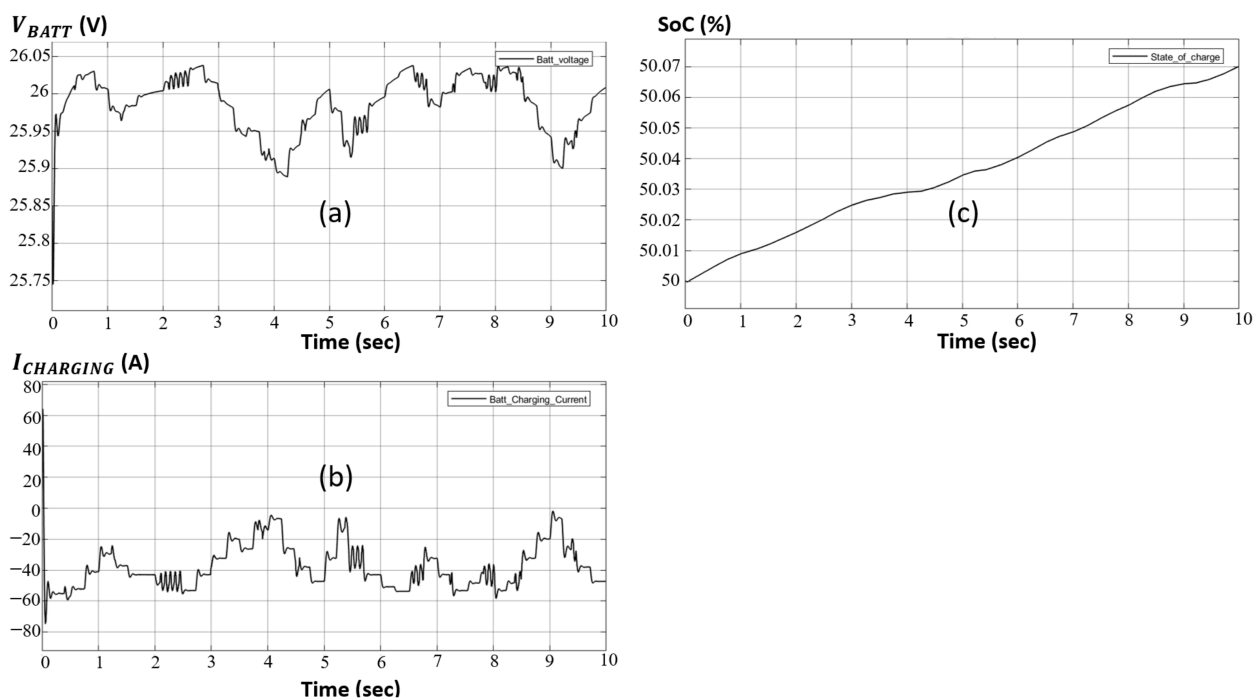


Figure 15. Battery's related curves under SIP1: (a) the battery voltage, (b) the battery charging current, and (c) the battery state of charge.

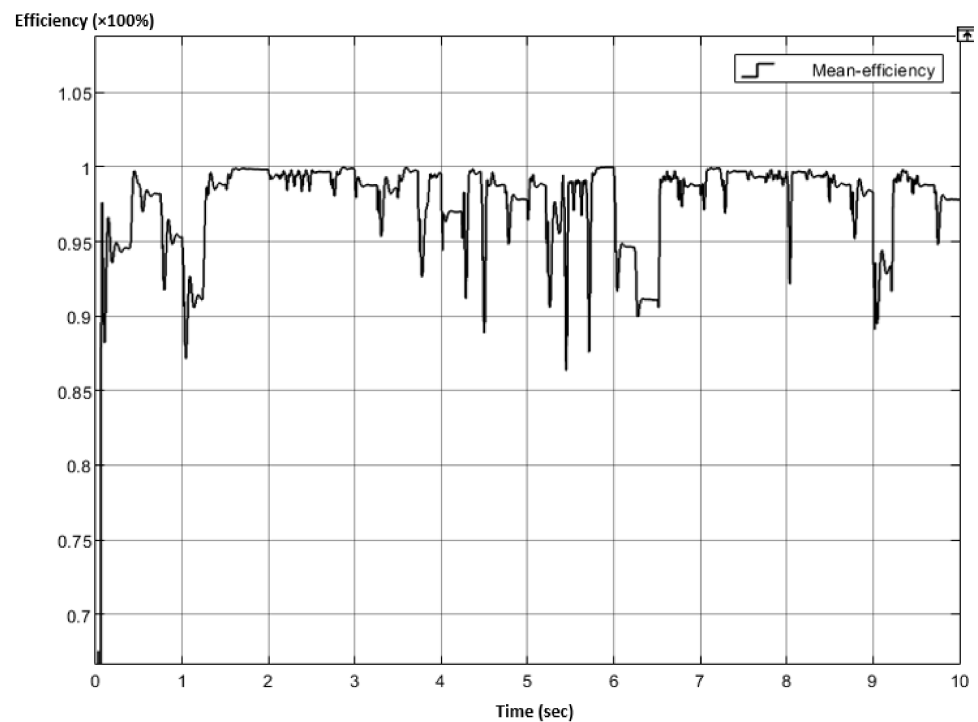


Figure 16. Mean efficiency (%) of the design under SIP1.

8.2. Results for SIP2

While switching the irradiance patterns to SIP2, the same circuit as in Figure 12, reflects different performance reactions, where the closeness between the actual and the ideal power curves is shown in Figure 17. The battery charging process, including the state of charge, the charging current, and the battery voltage, are expanded in Figure 18. The design mean efficiency particularly under SIP2 is shown in Figure 19.

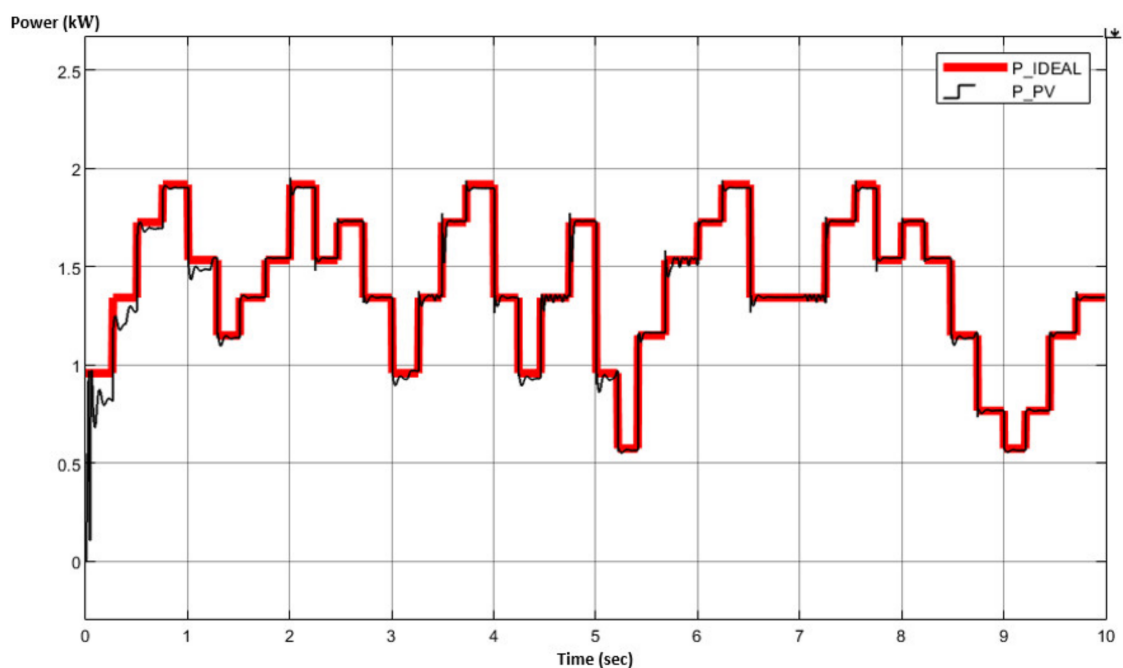


Figure 17. The alignment between the ideal and actual PV power curves (kWp) for SIP2.

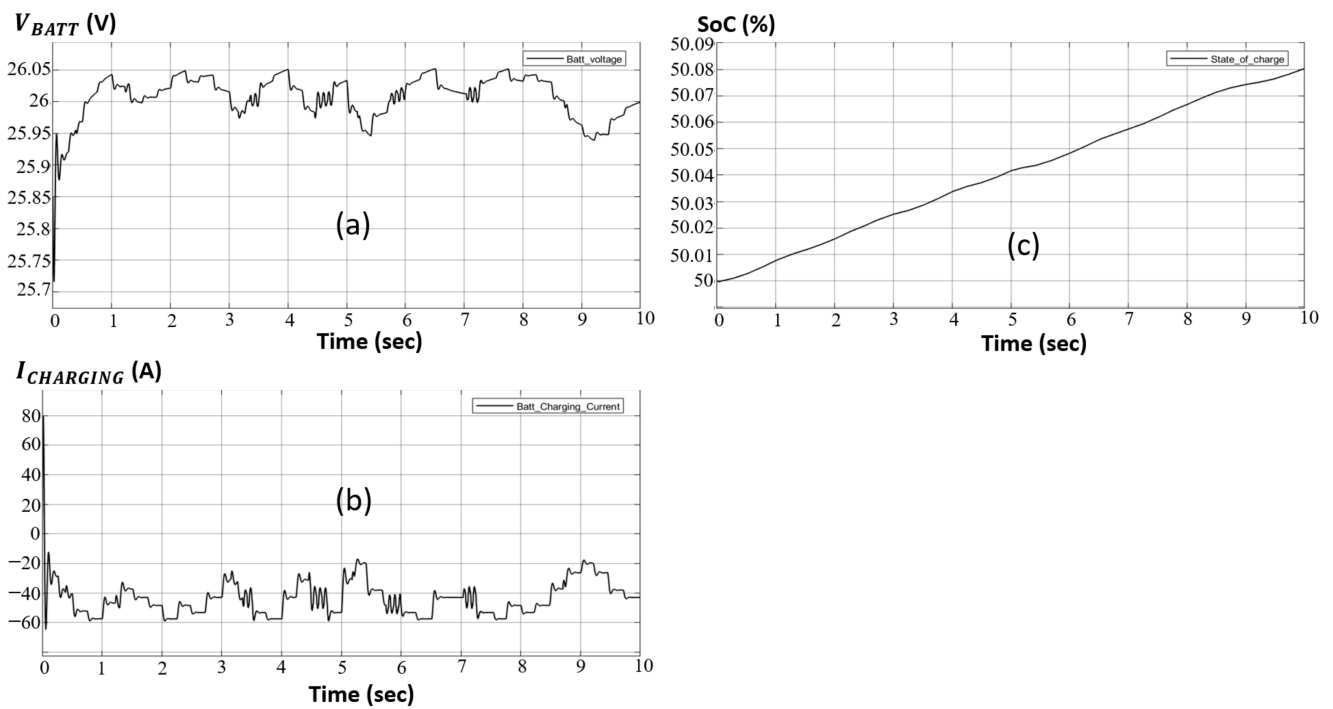


Figure 18. Battery's related curves under SIP2: (a) the battery voltage, (b) the battery charging current, and (c) the battery state of charge.

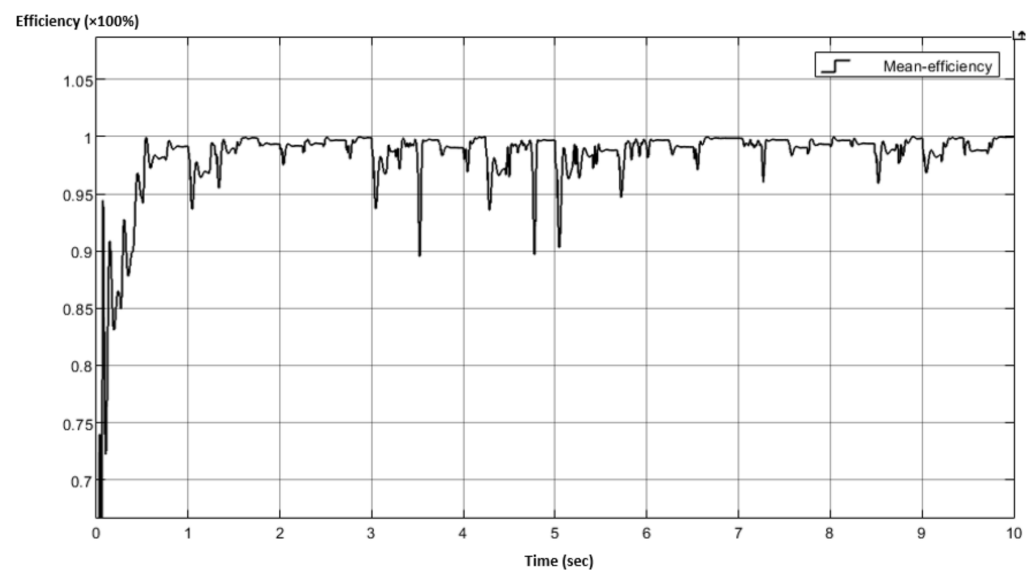


Figure 19. Mean efficiency (%) of the design under SIP2.

8.3. Results for SIP3

After switching the irradiance patterns to SIP3, Figure 20 shows the relevant closeness between the new actual and the ideal power curves. The battery charging process, including the state of charge, the charging current, and the battery voltage, are revealed in Figure 21. The design mean efficiency for SIP3 is shown in Figure 22.

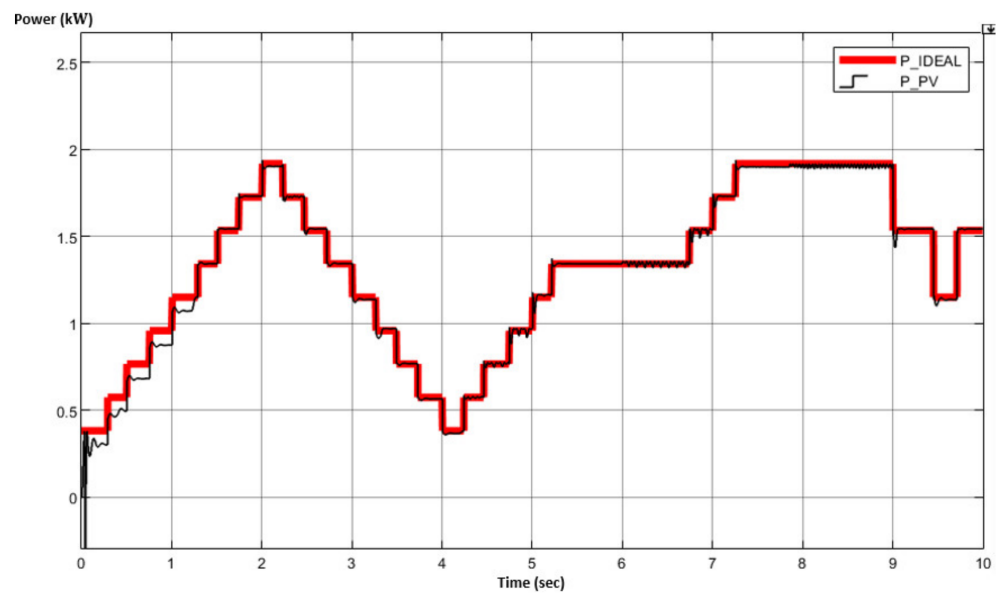


Figure 20. The alignment between the ideal and actual PV power curves (kWp) for SIP3.

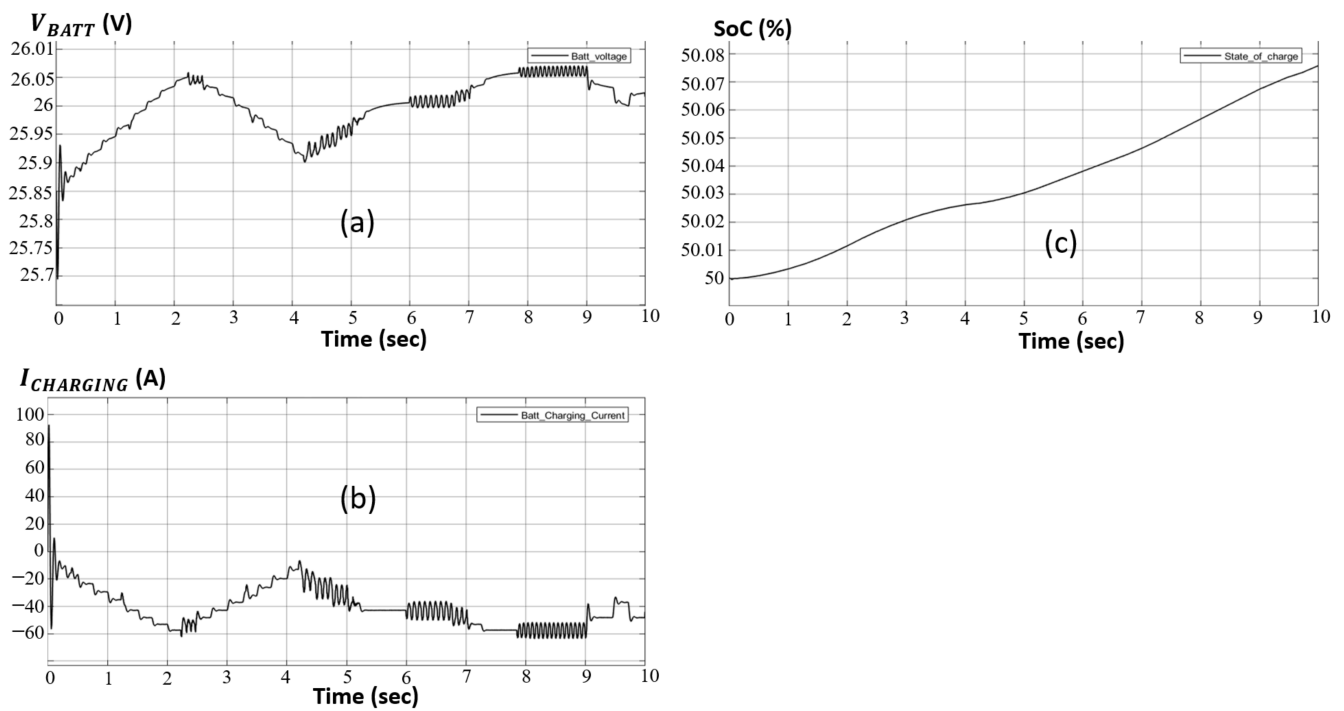


Figure 21. Battery’s related curves under SIP3: (a) the battery voltage, (b) the battery charging current, and (c) the battery state of charge.

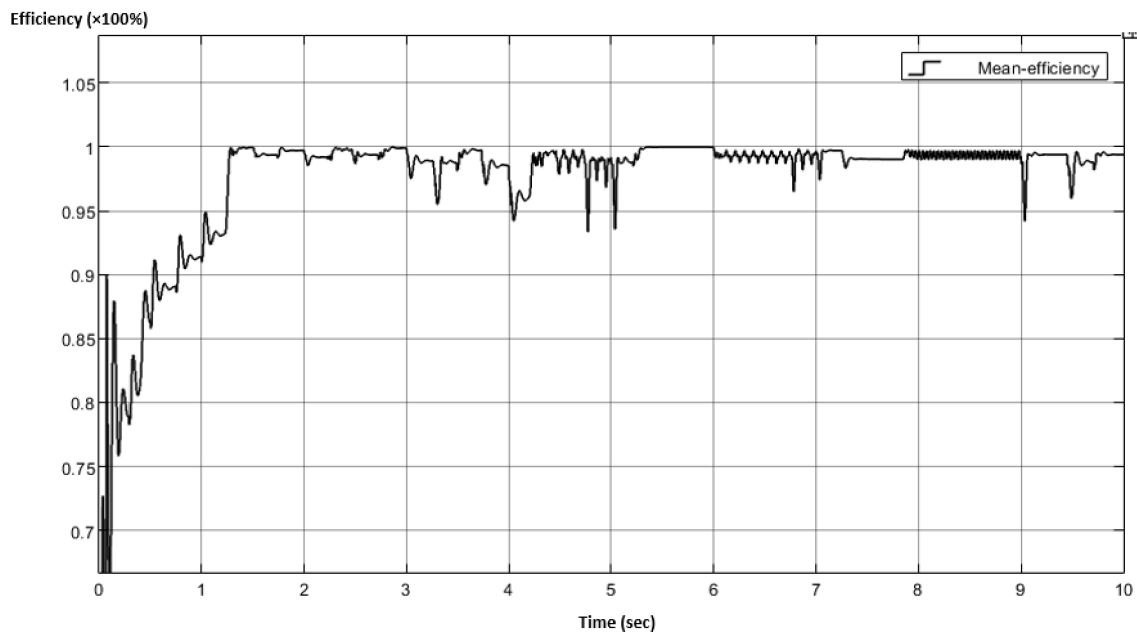


Figure 22. Mean efficiency (%) of the design under SIP3.

8.4. Results for SIP4

The SIP4 is applied to the same circuit design, where Figure 23 shows the alignment between the actual and the ideal power curves. Under the same conditions, Figure 24 encapsulates everything concerning the battery charging process, where finally in Figure 25, revealed is the mean efficiency for the design under SIP4 conditions.

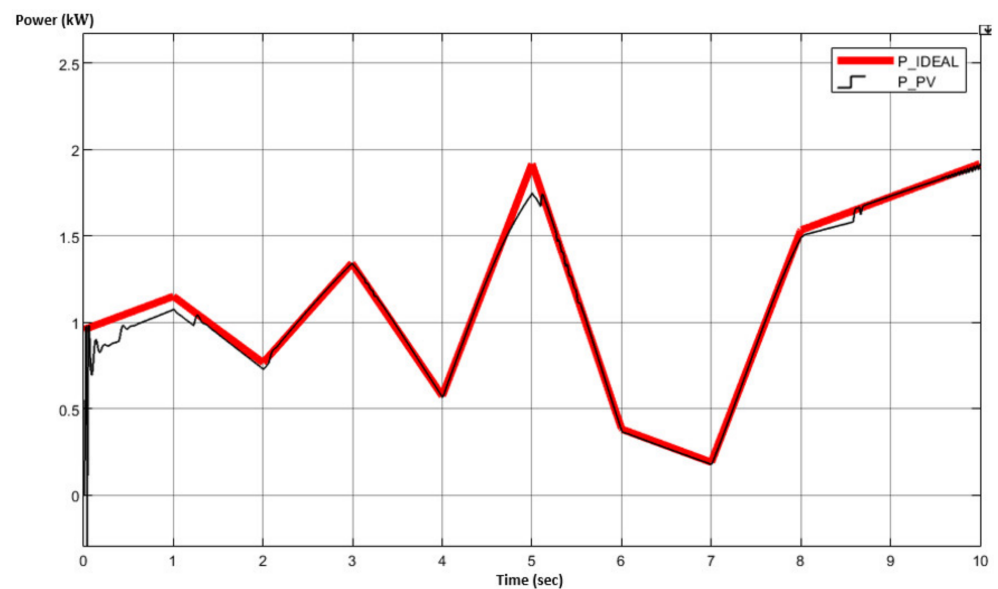


Figure 23. The alignment between the ideal and actual PV power curves (kWp) for SIP4.

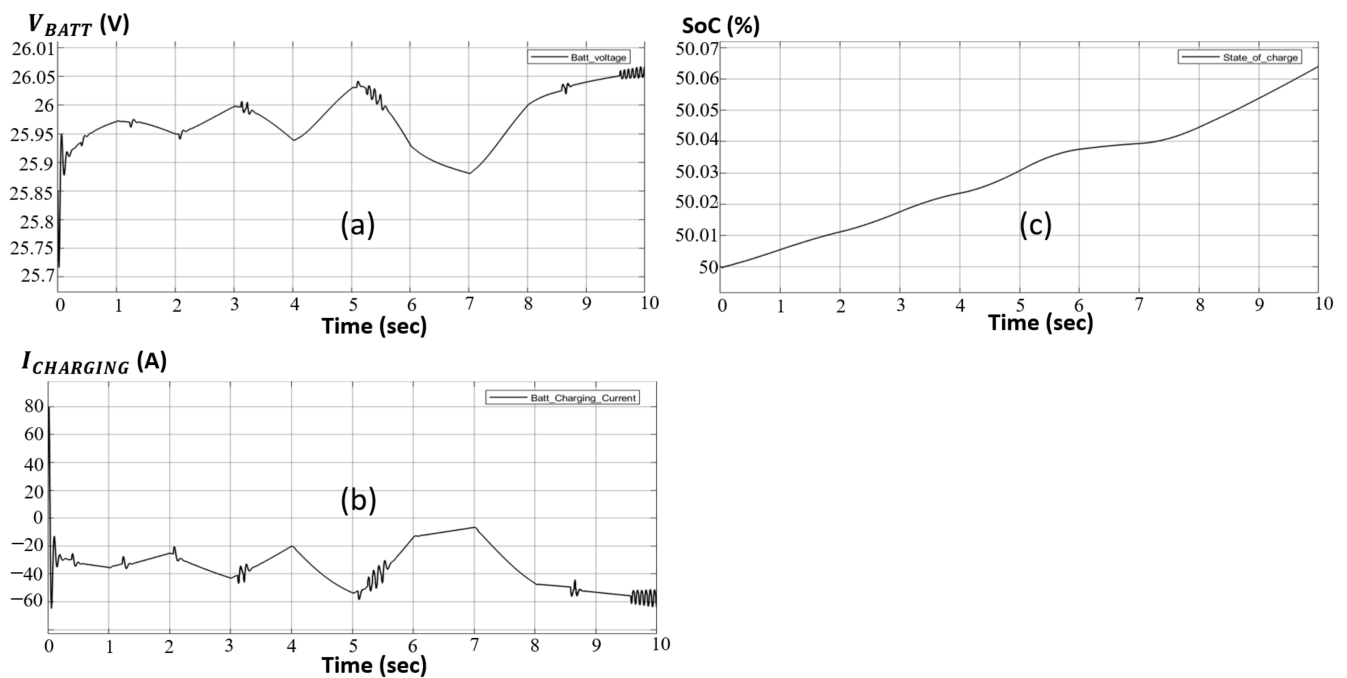


Figure 24. Battery's related curves under SIP4: (a) the battery voltage, (b) the battery charging current, and (c) the battery state of charge.

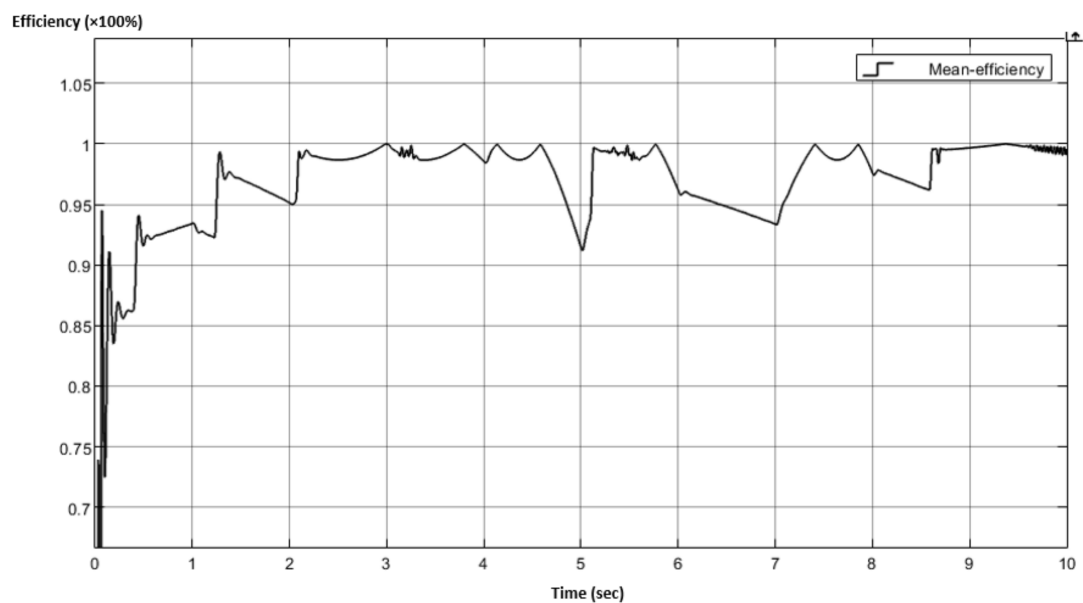


Figure 25. Mean efficiency (%) of the design under SIP4.

8.5. Results for Zero Irradiance (during Nights, etc.)

Instead of applying an actual time varying SIP, the design in this case is encountered with a zero irradiance, reflecting hence as null power output. The objective behind this exposure is to investigate the battery's charging process shown in Figure 26 and to detect whether the battery would be plugged off the circuit in case of a marginal state of discharge (i.e., $DoD \leq 25\%$).

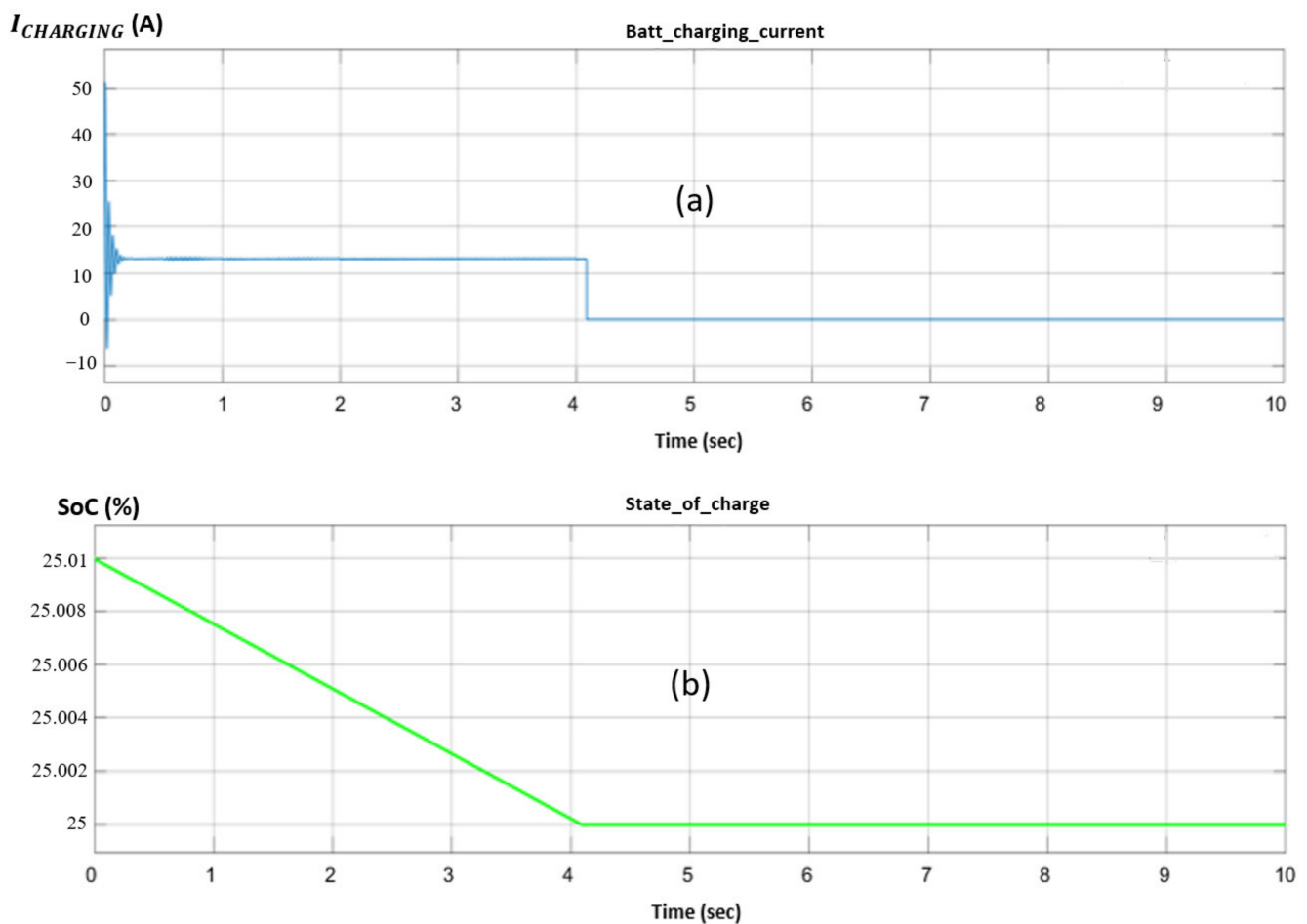


Figure 26. The battery's discharge current (a) and state of charge (b) under zero irradiance.

9. Discussion and Future Work

The overview of the different results for the investigated SIPs were satisfactory in general. Despite that the design has followed a regulation loop control, its response, however, did not constantly show an efficiency of 100%: this can be justified by the fact that the irradiance patterns are extremely fast (i.e., in order of 0.5 s), where the modified P&O algorithm cannot momentarily cope with. In other words, the obtained ideality factor was less than one, due to the computational speed of the proposed MPPT algorithm with respect to the SIP fluctuating speed. Beginning with SIP1, the mean efficiency ranged from 87% to 99.9%. This pattern in particular was the most complex, having the most rapidly fluctuating irradiance conditions with a time lapse of 0.5 s per variation. For SIP2, the mean efficiency ranged between 90% to 99.9%, where this pattern was less complex than the previous. In the case of SIP3, an increase in the mean efficiency is witnessed, where it ranged from 92% to 100%, such that the maximum efficiency scored from 93% to 100% for SIP4.

For each of the irradiance patterns, the SoC was continuously increasing, with modified slopes according to Figure 15, Figure 18, and Figure 21. The curve defining piece-wise slopes were directly based on the irradiance levels, where an increase in irradiance is reflected by a sharper upward directed line segment. As for the charging current, from the same figures, it can be noticed that its largest possible amount, supported by the PVA under specific irradiance values, is safely injected to the battery. The battery feeding voltage, also for all irradiance patterns, fluctuated between 25.9 V and 26.05 V, just as it was initially designed to be an output from the DC-DC interleaved synchronous buck converter. Accordingly, the battery under all irradiance circumstances would have the optimum safest feeding voltage (i.e., around 26 V) to be fed from.

For the case where there is not any irradiance (Figure 26, zero irradiance), the bi-directional DC-DC converter plugs out the battery when its SoC reaches 25%. The current value seen in Figure 26 is positive (according to the passive sign convention), meaning that no charging to the battery is occurring, but instead, current is being drawn from the battery. Within the same figure, where at $T = 4.2$ s, the SoC is equal to 25%. Successively to the right of this point, the SoC stabilizes at 0%, since the battery gets plugged out of the system for protective purposes (e.g., decelerate its aging process, saving its internal electrodes from excessive discharge, etc.). By taking into consideration what has been precedent, the contribution of this paper can be pointed out as follows:

1. The design has considered extreme irradiance fluctuations, with a time variance of 0.5 s, and irradiance intensity random variations from 100 W/m^2 to 1000 W/m^2 . Such irradiance fluctuations generally do not take place under real environmental conditions, regardless of the location of the PV systems' installation. Since the design has shown a good overall efficiency under such unrealistic irradiance conditions, it can be said that it should work as good or even better under actual irradiance conditions, when prototyped.
2. The synergistic cooperation between the modified P&O algorithm as well as the improved DC-DC converter resulted in minimal current/voltage ripples, thus, the voltage feeding/current injection to the battery are greatly smoothed.
3. The implemented low-threshold detection ability of the battery's SoC, and hence its conditional removal out of the system, protects its electrode from the effects of over-discharging, thus sustaining its expected lifecycle.

Moreover, the full set of sub-designs shown in Figure 12, can be industrialized into a real prototype, serving arrays of 1.918 kWp. The simplicity of algorithm implementation and power electronic converters, such as the DC-DC interleaved synchronous converter, and the bi-directional DC-DC converter offers the following advantages:

- Weight reduction of the gadgets: the smaller sizes of capacitors, inductors, etc. decreases the size of the entire system, making it more flexible for size-constraint applications.
- Financial reliability: the decreased complexities in the algorithms' establishments for different control sections of the design (i.e., MPPT control, current suppression, etc.), as well as the minimized components size, makes the overall design cost effective, and able to be manufactured without the need of special machinery and big industrial plants.
- Flexibility for improvement: while only modifying the power electronics items, the system could fit for larger PVA applications.
- Ability of hybridization: a set of this system could fit into multiple 3×3 PVA composing a PV farm, where the output of each is mutually injected to a DC grid as shown in Figure 27.

The industrialization of this design can be obtained and arranged in a Polyvinyl Chloride (PVC) enclosure, to improve its Ingress Protection (IP) rating, thus making it resilient in front of severe weather fluctuations as presented in Figure 28. The following list of items comprises its main backbone:

- Arduino: as a central processing unit, used to execute arithmetical procedures (calculation of power, etc.) as well as for the implementation of the modified MPPT algorithm.
- Liquid Crystal Display (LCD): this shall replace the scopes used during the simulation in Matlab/Simulink, thus offering a vivid physical display.
- Voltage/current sensors: used to captivate the real current/voltage quantities from the PVA. These sensors' data are then to be subjected to Analog to Digital Converters (ADC) to be inputted as discrete samples into the processor.
- Power electronic converters: implemented in Printed Circuit Boards (PCBs) in order to reduce space and facilitate connections.

- PVC enclosure: to cover the electronic boards of the design, making it waterproof and shock absorbent.

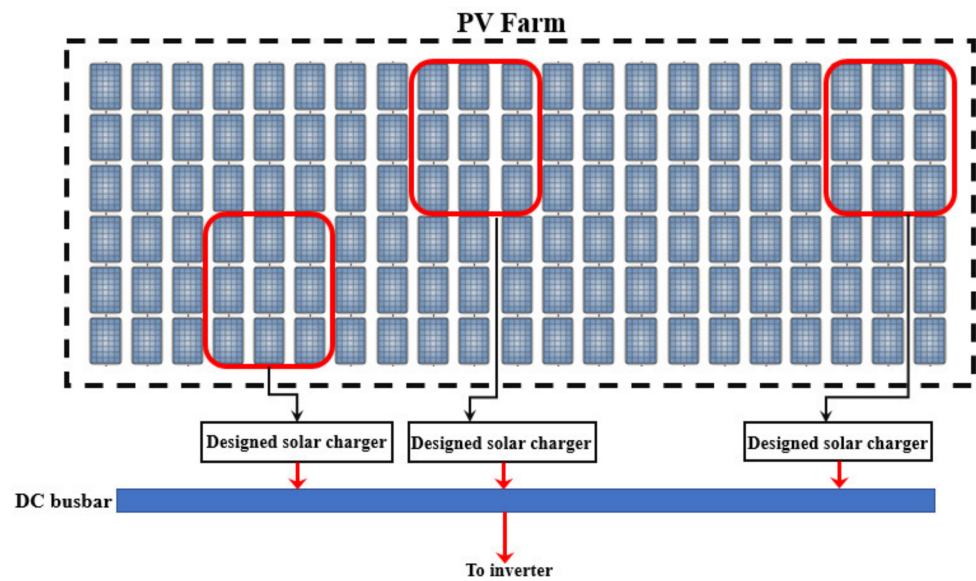


Figure 27. Expandability of the designed solar MPPT charger.

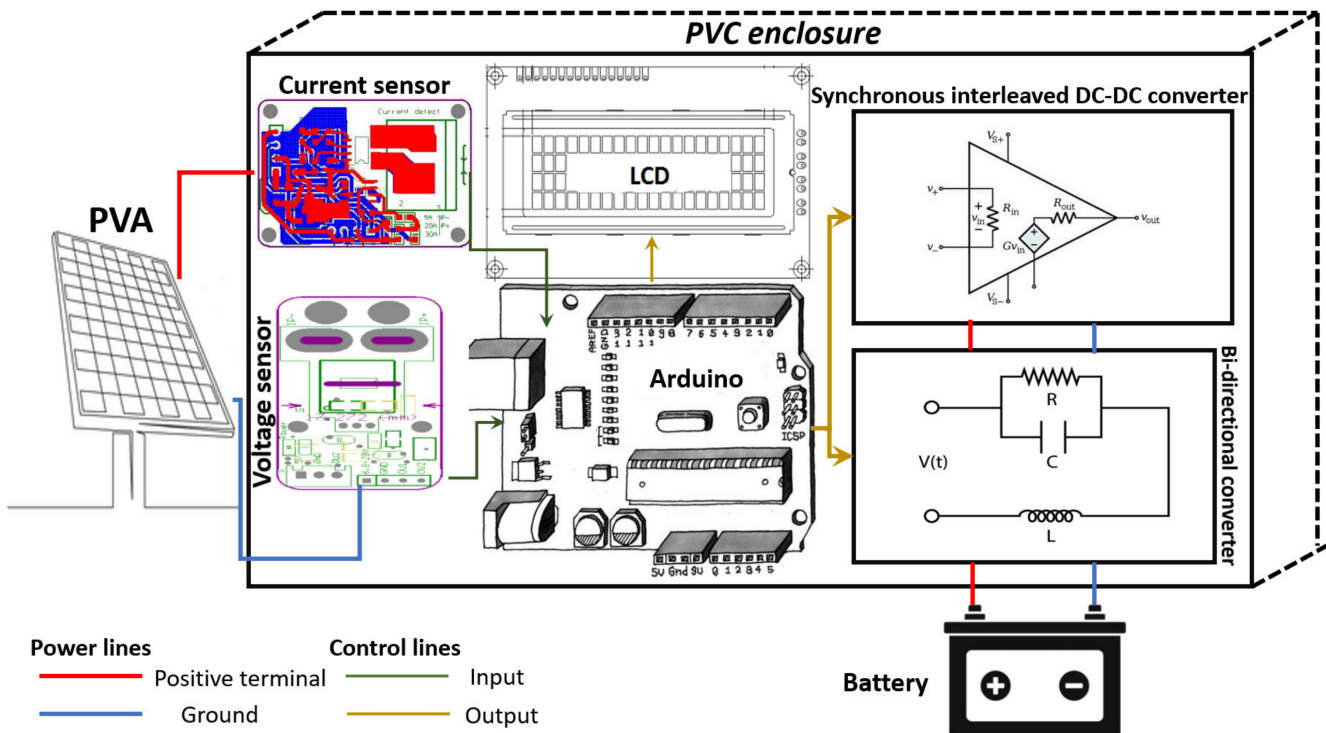


Figure 28. General overview of the suggested future design prototype.

10. Conclusions

This paper aimed to design an effective solar battery charger to be used in off-grid, standalone PV systems. After the setup of the 1.918 kWp PVA in SP configuration, an investigation is led for several SIPs, with fluctuating irradiances of 100 W/m^2 in 0.5 s time lapses. The novelty of the designed interleaved synchronous DC-DC converter granted smaller sizes of the needed inductors and capacitors, thus increasing the cost efficiency of the system. Low inductor ripple currents (20% of inductor current) with small output

voltage ripples (0.01 V) are obtained after the analysis of the output curves, furthering the design's simulation. The output of this converter hence produced a stubborn output voltage of 26 V, optimum to feed the 24 V, 150 Ah Li-I battery. For the sake of monitoring the battery charging current, a bi-directional DC-DC converter was successively used and controlled by I_{ref} method via a PI controller.

This in turn had led to a maximum safe charging current. At this stage, the V-I quantities are ensured to be at most optimum values, regardless of the irradiance fluctuations. In progress, a DoD control tactic was designed to ensure that the battery would never drain below 25% of complete charge, therefore sustaining its maximum life cycle. The mean efficiency of the MPPT ranged from a minimum of 87% to a maximum of 100%. In addition, this design has shown a flexibility in installation to adapt smaller/larger PV networks with a simple modification of the power electronics units. On the other side, and from a critical point of view, it can be said that the PVA of 1.918 kWp is too large to charge a battery of 150 Ah, but this was accounted for simulation purposes only. For instance, the designed DC-DC interleaved synchronous converter serves only to step down (i.e., Buck) the PVA's output voltage at a conventional range to feed the battery. Accordingly, this converter does not possess the ability to step up (i.e., Boost) the PVA's output voltage when it is below the recommended battery's voltage range. A better design would hence adopt both DC conversion techniques (i.e., Buck-Boost). The current design also did not encounter any partial shading conditions cases where it has only worked for uniform shading: the irradiance patterns, and despite their swift variations, are commonly objected to the entire PVA. In most real-world solar charging applications, designs are more often interfered with partial shading conditions, where the solar irradiance intensity over the PVA is inhomogeneous (i.e., some regions of the PVA receive more irradiance than others, and vice versa). This in turn lead to a more non-linearly disturbed P-V characteristic curve, in which the modified P&O would not function optimally. Another limitation of this work is that the PVA is always set under a working temperature of 25 °C, which is rarely the case for real-world PV applications: the temperature variations have also negative impacts on the P-V characteristic curve, where the modified P&O cannot also cope with.

As a final overview, this design has dealt with the process of Li-I battery charging, beginning with severe irradiance levels, to finally offering safe charging values at the fastest possible rate, while protecting the battery from accelerated ageing by a dedicated plug-out function. As for the future work, this model is encouraged to be manufactured and implemented in real-world PV applications, to furtherly analyze and investigate its real outcomes, when compared with the results obtained in this paper.

Author Contributions: Writing—original draft, K.O.; Writing—review & editing, A.H., M.A., T.L., B.C. and M.R.; Supervision, A.H., T.L., B.C. and M.R. All authors have read and agreed to the published version of the manuscript.

Funding: This research received no external funding.

Institutional Review Board Statement: Not applicable.

Informed Consent Statement: Not applicable.

Data Availability Statement: Data is unavailable due to privacy or ethical restrictions.

Conflicts of Interest: The authors declare no conflict of interest.

Nomenclature

Abbreviations

ADC	Analog to Digital Conversion
DC	Direct Current
DoD	Depth of Discharge
ESS	Energy Storage System
HC	Honey Comb

IGBT	Insulated Gate Bipolar Transistor
IP	Ingress Protection
LCD	Liquid Crystal Display
Li-I	Lithium-Ion
MOSFET	Metal Oxide Semi-conductor Field Effect Transistor
MPPT	Maximum Power Point Tracking
P&O	Perturb and Observe
PG	Proportional Gain
PCB	Printed Circuit Board
PI	Proportional Integral
PV	Photo Voltaic
PVA	PV Array
PVC	Polyvinyl Chloride
PVR	PV Reconfiguration
PWM	Pulse Width Modulation
SIP	Solar Irradiance Pattern
SoC	State of Charge
SP	Series Parallel
STC	Standard Test Conditions
TCT	Total Cross Tied
Units	
A	Ampere
s	Second
V	Volt
W	Watt
W/m ²	Irradiance, Watts per meter squared
Symbols	
CO ₂	Carbon dioxide
I_{BAT_CHARGE}	Battery charging current
I_{ref}	Reference current

References

- Pal, P.; Mukherjee, V.; Kumar, P.; Makhatha, M.E. Pre-feasibility analysis and performance assessment of solar photovoltaic (PV) modules for the application of renewable power generation. *Mater. Today Proc.* **2021**, *39*, 1813–1819. [\[CrossRef\]](#)
- Gielen, D.; Boshell, F.; Saygin, D.; Bazilian, M.D.; Wagner, N.; Gorini, R. The role of renewable energy in the global energy transformation. *Energy Strategy Rev.* **2019**, *24*, 38–50. [\[CrossRef\]](#)
- Boström, T.; Babar, B.; Hansen, J.B.; Good, C. The pure PV-EV energy system—A conceptual study of a nationwide energy system based solely on photovoltaics and electric vehicles. *Smart Energy* **2021**, *1*, 100001. [\[CrossRef\]](#)
- Li, G.; Shittu, S.; Diallo, T.M.O.; Yu, M.; Zhao, X.; Ji, J. A review of solar photovoltaic-thermoelectric hybrid system for electricity generation. *Energy* **2018**, *158*, 41–58. [\[CrossRef\]](#)
- Nwaigwe, K.; Mutabilwa, P.; Dintwa, E. An overview of solar power (PV systems) integration into electricity grids. *Mater. Sci. Energy Technol.* **2019**, *2*, 629–633. [\[CrossRef\]](#)
- Osmani, K.; Haddad, A.; Lemenand, T.; Castanier, B.; Ramadan, M. A review on maintenance strategies for PV systems. *Sci. Total. Environ.* **2020**, *746*, 141753. [\[CrossRef\]](#) [\[PubMed\]](#)
- Simonazzi, M.; Chiorboli, G.; Cova, P.; Menozzi, R.; Santoro, D.; Sapienza, S.; Sciancalepore, C.; Sozzi, G.; Delmonte, N. Smart soiling sensor for PV modules. *Microelectron. Reliab.* **2020**, *114*, 113789. [\[CrossRef\]](#)
- Osmani, K.; Ramadan, M.; Haddad, A.; Lemenand, T.; Castanier, B. A Short Review on Mathematical Algorithms for Predictive Maintenance Techniques and Anomaly Detection in PV Systems. In Proceedings of the 31st European Safety and Reliability Conference, ESREL, Angers, France, 19–23 September 2021; pp. 3222–3229.
- Pei, T.; Zhang, J.; Li, L.; Hao, X. A fault locating method for PV arrays based on improved voltage sensor placement. *Sol. Energy* **2020**, *201*, 279–297. [\[CrossRef\]](#)
- Pratt, L.; Govender, D.; Klein, R. Defect detection and quantification in electroluminescence images of solar PV modules using U-net semantic segmentation. *Renew. Energy* **2021**, *178*, 1211–1222. [\[CrossRef\]](#)
- Cole, W.; Greer, D.; Ho, J.; Margolis, R. Considerations for maintaining resource adequacy of electricity systems with high penetrations of PV and storage. *Appl. Energy* **2020**, *279*, 115795. [\[CrossRef\]](#)
- Majeed, R.; Waqas, A.; Sami, H.; Ali, M.; Shahzad, N. Experimental investigation of soiling losses and a novel cost-effective cleaning system for PV modules. *Sol. Energy* **2020**, *201*, 298–306. [\[CrossRef\]](#)
- Osmani, K.; Ramadan, M.; Haddad, A.; Lemenand, T.; Castanier, B. An Overview on the Use of Phase Change Material (PCM) for PV Cooling. *Key Eng. Mater.* **2022**, *922*, 3–9. [\[CrossRef\]](#)

14. de Oliveira, A.K.V.; Aghaei, M.; Rütther, R. Aerial infrared thermography for low-cost and fast fault detection in utility-scale PV power plants. *Sol. Energy* **2020**, *211*, 712–724. [[CrossRef](#)]
15. Alves, R.H.F.; Júnior, G.A.D.D.; Marra, E.G.; Lemos, R.P. Automatic fault classification in photovoltaic modules using Convolutional Neural Networks. *Renew. Energy* **2021**, *179*, 502–516. [[CrossRef](#)]
16. Maleki, A.; Haghighi, A.; Assad, M.E.H.; Mahariq, I.; Nazari, M.A. A review on the approaches employed for cooling PV cells. *Sol. Energy* **2020**, *209*, 170–185. [[CrossRef](#)]
17. Yurtseven, K.; Karatepe, E.; Deniz, E. Sensorless fault detection method for photovoltaic systems through mapping the inherent characteristics of PV plant site: Simple and practical. *Sol. Energy* **2021**, *216*, 96–110. [[CrossRef](#)]
18. Clavijo-Blanco, J.; Álvarez-Tey, G.; Saborido-Barba, N.; Barberá-González, J.; García-López, C.; Jiménez-Castañeda, R. Laboratory tests for the evaluation of the degradation of a photovoltaic plant of 2.85 MW_p with different classes of PV modules. *Renew. Energy* **2021**, *174*, 262–277. [[CrossRef](#)]
19. Li, C.; Yang, Y.; Zhang, K.; Zhu, C.; Wei, H. A fast MPPT-based anomaly detection and accurate fault diagnosis technique for PV arrays. *Energy Convers. Manag.* **2021**, *234*, 113950. [[CrossRef](#)]
20. Osmani, K.; Haddad, A.; Lemenand, T.; Castanier, B.; Ramadan, M. Material Based Fault Detection Methods for PV Systems. *Key Eng. Mater.* **2020**, *865*, 111–115. [[CrossRef](#)]
21. Abdulmunem, A.R.; Samin, P.M.; Rahman, H.A.; Hussien, H.A.; Mazali, I.I. Enhancing PV Cell's electrical efficiency using phase change material with copper foam matrix and multi-walled carbon nanotubes as passive cooling method. *Renew. Energy* **2020**, *160*, 663–675. [[CrossRef](#)]
22. Ameer, A.; Berrada, A.; Loudiyi, K.; Aggour, M. Forecast modeling and performance assessment of solar PV systems. *J. Clean. Prod.* **2020**, *267*, 122167. [[CrossRef](#)]
23. Fares, E.; Bicer, Y. Comparative performance evaluation of c-Si and GaAs type PV cells with and without anti-soiling coating using energy and exergy analysis. *Renew. Energy* **2020**, *146*, 1010–1020. [[CrossRef](#)]
24. Thopil, G.A.; Sachse, C.E.; Lalk, J.; Thopil, M.S. Techno-economic performance comparison of crystalline and thin film PV panels under varying meteorological conditions: A high solar resource southern hemisphere case. *Appl. Energy* **2020**, *275*, 115041. [[CrossRef](#)]
25. Mirzaei, M.; Mohiabadi, M.Z. A comparative analysis of long-term field test of monocrystalline and polycrystalline PV power generation in semi-arid climate conditions. *Energy Sustain. Dev.* **2017**, *38*, 93–101. [[CrossRef](#)]
26. Brecl, K.; Bokalič, M.; Topič, M. Annual energy losses due to partial shading in PV modules with cut wafer-based Si solar cells. *Renew. Energy* **2021**, *168*, 195–203. [[CrossRef](#)]
27. Ansari, M.I.H.; Qurashi, A.; Nazeeruddin, M.K. Frontiers, opportunities, and challenges in perovskite solar cells: A critical review. *J. Photochem. Photobiol. C Photochem. Rev.* **2018**, *35*, 1–24. [[CrossRef](#)]
28. Sultan, S.; Kim, J.H.; Kim, S.; Kwon, Y.; Lee, J.S. Innovative strategies toward challenges in PV-powered electrochemical CO₂ reduction. *J. Energy Chem.* **2021**, *60*, 410–416. [[CrossRef](#)]
29. Babajide, A.; Brito, M.C. Solar PV systems to eliminate or reduce the use of diesel generators at no additional cost: A case study of Lagos, Nigeria. *Renew. Energy* **2021**, *172*, 209–218. [[CrossRef](#)]
30. Ghadikolaie, S.S.C. An enviroeconomic review of the solar PV cells cooling technology effect on the CO₂ emission reduction. *Sol. Energy* **2021**, *216*, 468–492. [[CrossRef](#)]
31. Gómez-Navarro, T.; Brazzini, T.; Alfonso-Solar, D.; Vargas-Salgado, C. Analysis of the potential for PV rooftop prosumer production: Technical, economic and environmental assessment for the city of Valencia (Spain). *Renew. Energy* **2021**, *174*, 372–381. [[CrossRef](#)]
32. Wang, M.; Mao, X.; Gao, Y.; He, F. Potential of carbon emission reduction and financial feasibility of urban rooftop photovoltaic power generation in Beijing. *J. Clean. Prod.* **2018**, *203*, 1119–1131. [[CrossRef](#)]
33. Gil, G.O.; Chowdhury, J.I.; Balta-Ozkan, N.; Hu, Y.; Varga, L.; Hart, P. Optimising renewable energy integration in new housing developments with low carbon technologies. *Renew. Energy* **2021**, *169*, 527–540. [[CrossRef](#)]
34. Dutta, R. *Use of Clean, Renewable and Alternative Energies in Mitigation of Greenhouse Gases*; Elsevier: Amsterdam, The Netherlands, 2020; Volume 3, pp. 821–834. [[CrossRef](#)]
35. Razmjoo, A.; Kaigutha, L.G.; Rad, M.A.V.; Marzband, M.; Davarpanah, A.; Denai, M. A Technical analysis investigating energy sustainability utilizing reliable renewable energy sources to reduce CO₂ emissions in a high potential area. *Renew. Energy* **2021**, *164*, 46–57. [[CrossRef](#)]
36. Huuki, H.; Karhinen, S.; Böök, H.; Ding, C.; Ruokamo, E. Residential solar power profitability with thermal energy storage and carbon-corrected electricity prices. *Util. Policy* **2021**, *68*, 101157. [[CrossRef](#)]
37. Akinsipe, O.C.; Moya, D.; Kaparaju, P. Design and economic analysis of off-grid solar PV system in Jos-Nigeria. *J. Clean. Prod.* **2021**, *287*, 125055. [[CrossRef](#)]
38. Osmani, K.; Haddad, A.; Jaber, H.; Lemenand, T.; Castanier, B.; Ramadan, M. Mitigating the effects of partial shading on PV system's performance through PV array reconfiguration: A review. *Therm. Sci. Eng. Prog.* **2022**, *31*, 101280. [[CrossRef](#)]
39. Al-Addous, M.; Dalala, Z.; Class, C.B.; Alawneh, F.; Al-Taani, H. Performance analysis of off-grid PV systems in the Jordan Valley. *Renew. Energy* **2017**, *113*, 930–941. [[CrossRef](#)]
40. Grande, L.S.A.; Yahyaoui, I.; Gómez, S.A. Energetic, economic and environmental viability of off-grid PV-BESS for charging electric vehicles: Case study of Spain. *Sustain. Cities Soc.* **2018**, *37*, 519–529. [[CrossRef](#)]

41. Satpathy, R.; Pamuru, V. *Chapter 7—Off-Grid Solar Photovoltaic Systems. Solar PV Power Design, Manufacturing and Applications from Sand to Systems*; Academic Press: Cambridge, MA, USA, 2021; pp. 267–315.
42. Osmani, K.; Ramadan, M.; Lemenand, T.; Castanier, B.; Haddad, A. Optimization of PV array tilt angle for minimum levelized cost of energy. *Comput. Electr. Eng.* **2021**, *96*, 107474. [[CrossRef](#)]
43. Said, Z.; Mehmood, A.; Waqas, A.; Hachicha, A.A.; Loni, R. Central versus off-grid photovoltaic system, the optimal option for the domestic sector based on techno-economic-environmental assessment for United Arab Emirates. *Sustain. Energy Technol. Assess.* **2021**, *43*, 100944.
44. Mulleriyawage, U.G.K.; Shen, W.X. Optimally sizing of battery energy storage capacity by operational optimization of residential PV-Battery systems: An Australian household case study. *Renew. Energy* **2020**, *160*, 852–864. [[CrossRef](#)]
45. El Kafazi, I.; Lafkih, M.; Bannari, R. PV generator and energy storage systems for laboratory building. *Energy Rep.* **2020**, *6*, 672–679. [[CrossRef](#)]
46. Barzegkar-Ntovom, G.; Chatzigeorgiou, N.G.; Nousdilis, A.I.; Vomva, S.A.; Kryonidis, G.C.; Kontis, E.O.; Georghiou, G.E.; Christoforidis, G.C.; Papagiannis, G.K. Assessing the viability of battery energy storage systems coupled with photovoltaics under a pure self-consumption scheme. *Renew. Energy* **2020**, *152*, 1302–1309. [[CrossRef](#)]
47. Wang, Y.; Das, R.; Putrus, G.; Kotter, R. Economic evaluation of photovoltaic and energy storage technologies for future domestic energy systems—A case study of the UK. *Energy* **2020**, *203*, 117826. [[CrossRef](#)]
48. Osmani, K.; Alkhedher, M.; Ramadan, M.; Choi, D.S.; Li, L.K.; Doranehgard, M.H.; Olabi, A.-G. Recent progress in the thermal management of lithium-ion batteries. *J. Clean. Prod.* **2023**, *389*, 136024. [[CrossRef](#)]
49. Liu, J.; Chen, X.; Yang, H.; Li, Y. Energy storage and management system design optimization for a photovoltaic integrated low-energy building. *Energy* **2020**, *190*, 116424. [[CrossRef](#)]
50. Yu, H.J.J. System contributions of residential battery systems: New perspectives on PV self-consumption. *Energy Econ.* **2021**, *96*, 105151. [[CrossRef](#)]
51. Aniello, G.; Shamon, H.; Kuckshinrichs, W. Micro-economic assessment of residential PV and battery systems: The underrated role of financial and fiscal aspects. *Appl. Energy* **2021**, *281*, 115667. [[CrossRef](#)]
52. Alsolami, M. A multi-input, multi-stage step-up DC-DC converter for PV applications. *Alex. Eng. J.* **2021**, *60*, 2315–2324. [[CrossRef](#)]
53. Raj, A.; Arya, S.R.; Gupta, J. Solar PV array-based DC-DC converter with MPPT for low power applications. *Renew. Energy Focus* **2020**, *34*, 109–119. [[CrossRef](#)]
54. Kumar, L.A.; Alexander, S.A.; Rajendran, M. *Power Electronic Converters for Solar Photovoltaic Systems*; Academic Press: Cambridge, MA, USA, 2021; pp. 207–234.
55. Celikel, R.; Yilmaz, M.; Gundogdu, A. A voltage scanning-based MPPT method for PV power systems under complex partial shading conditions. *Renew. Energy* **2022**, *184*, 361–373. [[CrossRef](#)]
56. Mirzaei, A.; Rezvanyvardom, M. High voltage gain soft switching full bridge interleaved Flyback DC-DC converter for PV applications. *Sol. Energy* **2020**, *196*, 217–227. [[CrossRef](#)]
57. Revathi, B.S.; Mahalingam, P.; Gonzalez-Longatt, F. Interleaved high gain DC-DC converter for integrating solar PV source to DC bus. *Sol. Energy* **2019**, *188*, 924–934. [[CrossRef](#)]
58. Cibira, G. PV cell electrical parameters dynamic modelling based on double-diode five-parameter reduced forms. *Appl. Surf. Sci.* **2018**, *461*, 98–101. [[CrossRef](#)]
59. Barth, N.; Jovanovic, R.; Ahzi, S.; Khaleel, M.A. PV panel single and double diode models: Optimization of the parameters and temperature dependence. *Sol. Energy Mater. Sol. Cells* **2016**, *148*, 87–98. [[CrossRef](#)]
60. de Oliveira, I.; Capovilla, D.A.; Moura, A.L.; Timóteo, V.S.; Carvalho, J.F.; Frejlich, J. Nonlinear photovoltaic effect in Sillenite photorefractive crystals. *Opt. Mater.* **2017**, *66*, 72–78. [[CrossRef](#)]
61. Wang, J.; Yang, B.; Li, D.; Zeng, C.; Chen, Y.; Guo, Z.; Zhang, X.; Tan, T.; Shu, H.; Yu, T. Photovoltaic cell parameter estimation based on improved equilibrium optimizer algorithm. *Energy Convers. Manag.* **2021**, *236*, 114051. [[CrossRef](#)]
62. Archila, L.M.P.; Rodríguez, J.D.B.; Correa, R. Implicit modelling of series-parallel photovoltaic arrays using double-diode model and its solution. *Sol. Energy* **2021**, *214*, 131–137. [[CrossRef](#)]
63. Amir, A.; Che, H.S.; Amir, A.; El Khateb, A.; Rahim, N.A. Transformerless high gain boost and buck-boost DC-DC converters based on extendable switched capacitor (SC) cell for stand-alone photovoltaic system. *Sol. Energy* **2018**, *171*, 212–222. [[CrossRef](#)]
64. Saravanan, S.; Babu, N.R. A modified high step-up non-isolated DC-DC converter for PV application. *J. Appl. Res. Technol.* **2017**, *15*, 242–249. [[CrossRef](#)]
65. Revathi, B.S.; Prabhakar, M. Non isolated high gain DC-DC converter topologies for PV applications—A comprehensive review. *Renew. Sustain. Energy Rev.* **2016**, *66*, 920–933. [[CrossRef](#)]
66. Tewari, N.; Sreedevi, V. A novel single switch dc-dc converter with high voltage gain capability for solar PV based power generation systems. *Sol. Energy* **2018**, *171*, 466–477. [[CrossRef](#)]
67. Dileep, G.; Singh, S. Selection of non-isolated DC-DC converters for solar photovoltaic system. *Renew. Sustain. Energy Rev.* **2017**, *76*, 1230–1247. [[CrossRef](#)]
68. Van De Sande, W.; Ravyts, S.; Sangwongwanich, A.; Manganiello, P.; Yang, Y.; Blaabjerg, F.; Driesen, J.; Daenen, M. A mission profile-based reliability analysis framework for photovoltaic DC-DC converters. *Microelectron. Reliab.* **2019**, *101*, 113383. [[CrossRef](#)]

69. Amir, A.; Amir, A.; Che, H.S.; Elkhateb, A.; Rahim, N.A. Comparative analysis of high voltage gain DC-DC converter topologies for photovoltaic systems. *Renew. Energy* **2019**, *136*, 1147–1163. [[CrossRef](#)]
70. Anita, S.J.; Ahmed, Y.S.; Prabhu, D.H.; Govind, S. Proposed modified solar based dc-dc quadratic boost converter for modern irrigation system. *Mater. Today: Proc.* **2020**, *33*, 4656–4662. [[CrossRef](#)]
71. Yang, Y.; Wu, Q.; Lin, W.; Chi, X.; Liu, D.; Jiang, A. Design and Simulation of a Kind of Wide, High Input Voltage DC-DC Converter for PV. *IFAC-PapersOnLine* **2017**, *50*, 2125–2130. [[CrossRef](#)]
72. Rezvanyvardom, M.; Mirzaei, A. High gain configuration of modified ZVT SEPIC-Boost DC-DC converter with coupled inductors for photovoltaic applications. *Sol. Energy* **2020**, *208*, 357–367. [[CrossRef](#)]
73. Mirza, A.F.; Ling, Q.; Javed, M.Y.; Mansoor, M. Novel MPPT techniques for photovoltaic systems under uniform irradiance and Partial shading. *Sol. Energy* **2019**, *184*, 628–648. [[CrossRef](#)]
74. Behera, M.K.; Saikia, L.C. A new combined extreme learning machine variable steepest gradient ascent MPPT for PV system based on optimized PI-FOI cascade controller under uniform and partial shading conditions. *Sustain. Energy Technol. Assess.* **2020**, *42*, 100859. [[CrossRef](#)]
75. Kamran, M.; Mudassar, M.; Fazal, M.R.; Asghar, M.U.; Bilal, M.; Asghar, R. Implementation of improved Perturb & Observe MPPT technique with confined search space for standalone photovoltaic system. *J. King Saud Univ.—Eng. Sci.* **2020**, *32*, 432–441. [[CrossRef](#)]
76. Abdel-Salam, M.; El-Mohandes, M.-T.; Goda, M. An improved perturb-and-observe based MPPT method for PV systems under varying irradiation levels. *Sol. Energy* **2018**, *171*, 547–561. [[CrossRef](#)]
77. Devi, V.K.; Premkumar, K.; Beevi, A.B.; Ramaiyer, S. A modified Perturb & Observe MPPT technique to tackle steady state and rapidly varying atmospheric conditions. *Sol. Energy* **2017**, *157*, 419–426. [[CrossRef](#)]
78. Ahmed, J.; Salam, Z. An improved perturb and observe (P&O) maximum power point tracking (MPPT) algorithm for higher efficiency. *Appl. Energy* **2015**, *150*, 97–108. [[CrossRef](#)]
79. Shahid, H.; Kamran, M.; Mehmood, Z.; Saleem, M.Y.; Mudassar, M.; Haider, K. Implementation of the novel temperature controller and incremental conductance MPPT algorithm for indoor photovoltaic system. *Sol. Energy* **2018**, *163*, 235–242. [[CrossRef](#)]
80. Tey, K.S.; Mekhilef, S. Modified incremental conductance MPPT algorithm to mitigate inaccurate responses under fast-charging solar irradiation level. *Sol. Energy* **2014**, *101*, 333–342. [[CrossRef](#)]
81. Murtaza, A.; Chiaberge, M.; Spertino, F.; Shami, U.T.; Boero, D.; De Giuseppe, M. MPPT technique based on improved evaluation of photovoltaic parameters for uniformly irradiated photovoltaic array. *Electr. Power Syst. Res.* **2017**, *145*, 248–263. [[CrossRef](#)]
82. Das, P. Maximum Power Tracking Based Open Circuit Voltage Method for PV System. *Energy Procedia* **2016**, *90*, 2–13. [[CrossRef](#)]
83. Fares, D.; Fathi, M.; Shams, I.; Mekhilef, S. A novel global MPPT technique based on squirrel search algorithm for PV module under partial shading conditions. *Energy Convers. Manag.* **2021**, *230*, 113773. [[CrossRef](#)]
84. Zhao, Z.; Cheng, R.; Yan, B.; Zhang, J.; Zhang, Z.; Zhang, M.; Lai, L.L. A dynamic particles MPPT method for photovoltaic systems under partial shading conditions. *Energy Convers. Manag.* **2020**, *220*, 113070. [[CrossRef](#)]
85. Mansoor, M.; Mirza, A.F.; Ling, Q. Harris hawk optimization-based MPPT control for PV systems under partial shading conditions. *J. Clean. Prod.* **2020**, *274*, 122857. [[CrossRef](#)]
86. Mansoor, M.; Mirza, A.F.; Ling, Q.; Javed, M.Y. Novel Grass Hopper optimization based MPPT of PV systems for complex partial shading conditions. *Sol. Energy* **2020**, *198*, 499–518. [[CrossRef](#)]
87. Senthilvel, A.; Vijeyakumar, K.; Vinothkumar, B. FPGA based implementation of MPPT algorithms for photovoltaic system under partial shading conditions. *Microprocess. Microsyst.* **2020**, *77*, 103011. [[CrossRef](#)]
88. Mirza, A.F.; Mansoor, M.; Ling, Q.; Yin, B.; Javed, M.Y. A Salp-Swarm Optimization based MPPT technique for harvesting maximum energy from PV systems under partial shading conditions. *Energy Convers. Manag.* **2020**, *209*, 112625. [[CrossRef](#)]
89. Titri, S.; Larbes, C.; Toumi, K.Y.; Benatchba, K. A new MPPT controller based on the Ant colony optimization algorithm for Photovoltaic systems under partial shading conditions. *Appl. Soft Comput.* **2017**, *58*, 465–479. [[CrossRef](#)]
90. da Rocha, M.V.; Sampaio, L.P.; da Silva, S.A.O. Comparative analysis of MPPT algorithms based on Bat algorithm for PV systems under partial shading condition. *Sustain. Energy Technol. Assess.* **2020**, *40*, 100761. [[CrossRef](#)]
91. Fathy, A.; Rezk, H.; Yousri, D. A robust global MPPT to mitigate partial shading of triple-junction solar cell-based system using manta ray foraging optimization algorithm. *Sol. Energy* **2020**, *207*, 305–316. [[CrossRef](#)]
92. Pal, R.S.; Mukherjee, V. Metaheuristic based comparative MPPT methods for photovoltaic technology under partial shading condition. *Energy* **2020**, *212*, 118592. [[CrossRef](#)]
93. Avila, L.; De Paula, M.; Trimboli, M.; Carlucho, I. Deep reinforcement learning approach for MPPT control of partially shaded PV systems in Smart Grids. *Appl. Soft Comput.* **2020**, *97*, 106711. [[CrossRef](#)]
94. Laxman, B.; Annamraju, A.; Srikanth, N.V. A grey wolf optimized fuzzy logic based MPPT for shaded solar photovoltaic systems in microgrids. *Int. J. Hydrog. Energy* **2021**, *46*, 10653–10665. [[CrossRef](#)]
95. Charin, C.; Ishak, D.; Zainuri, M.A.A.M.; Ismail, B.; Jamil, M.K.M. A hybrid of bio-inspired algorithm based on Levy flight and particle swarm optimizations for photovoltaic system under partial shading conditions. *Sol. Energy* **2021**, *217*, 1–14. [[CrossRef](#)]
96. Mohapatra, A.; Nayak, B.; Das, P.; Mohanty, K.B. A review on MPPT techniques of PV system under partial shading condition. *Renew. Sustain. Energy Rev.* **2017**, *80*, 854–867. [[CrossRef](#)]
97. Diab, A.A.Z.; Rezk, H. Global MPPT based on flower pollination and differential evolution algorithms to mitigate partial shading in building integrated PV system. *Sol. Energy* **2017**, *157*, 171–186. [[CrossRef](#)]

98. Yang, B.; Zhong, L.; Zhang, X.; Shu, H.; Yu, T.; Li, H.; Jiang, L.; Sun, L. Novel bio-inspired memetic salp swarm algorithm and application to MPPT for PV systems considering partial shading condition. *J. Clean. Prod.* **2019**, *215*, 1203–1222. [[CrossRef](#)]
99. Jose, B.K. Fuzzy Based Maximum Power Point Tracking of PV Array under Non-uniform Irradiance Conditions. *Mater. Today Proc.* **2020**, *24*, 1835–1842. [[CrossRef](#)]
100. Bharathi, K.; Sasikumar, M. Power flow control based on bidirectional converter for hybrid power generation system using microcontroller. *Microprocess. Microsyst.* **2021**, *82*, 103950. [[CrossRef](#)]
101. Siva Reddy, R.V. Microcontroller based bidirectional buck–boost converter for photo-voltaic power plant. *J. Electr. Syst. Inf. Technol.* **2018**, *5*, 745–758. [[CrossRef](#)]
102. Kanta, S.; Plangklang, B.; Subsingha, W. Design of a Bi-directional DC-DC 4 Phase Interleave Converter for PV Applications. *Energy Procedia* **2014**, *56*, 604–609. [[CrossRef](#)]
103. Chu, G.; Wen, H.; Jiang, L.; Hu, Y.; Li, X. Bidirectional flyback based isolated-port submodule differential power processing optimizer for photovoltaic applications. *Sol. Energy* **2017**, *158*, 929–940. [[CrossRef](#)]
104. Spier, D.; Oggier, G.; da Silva, S. Dynamic modeling and analysis of the bidirectional DC-DC boost-buck converter for renewable energy applications. *Sustain. Energy Technol. Assess.* **2019**, *34*, 133–145. [[CrossRef](#)]
105. Mao, M.; Zhang, L.; Yang, L.; Chong, B.; Huang, H.; Zhou, L. MPPT using modified salp swarm algorithm for multiple bidirectional PV-Cuk converter system under partial shading and module mismatch. *Sol. Energy* **2020**, *209*, 334–349. [[CrossRef](#)]
106. Kumar, L.A.; Alexander, S.A.; Rajendran, M. *Power Electronic Converters for Solar Photovoltaic Systems*; Academic Press: Cambridge, MA, USA, 2021; pp. 235–288.
107. Ajmal, A.M.; Babu, T.S.; Ramachandaramurthy, V.K.; Yousri, D.; Ekanayake, J.B. Static and dynamic reconfiguration approaches for mitigation of partial shading influence in photovoltaic arrays. *Sustain. Energy Technol. Assess.* **2020**, *40*, 100738. [[CrossRef](#)]
108. Yadav, A.S.; Mukherjee, V. Conventional and advanced PV array configurations to extract maximum power under partial shading conditions: A review. *Renew. Energy* **2021**, *178*, 977–1005. [[CrossRef](#)]
109. Krishna, G.S.; Moger, T. Reconfiguration strategies for reducing partial shading effects in photovoltaic arrays: State of the art. *Sol. Energy* **2019**, *182*, 429–452. [[CrossRef](#)]
110. Yadav, V.K.; Yadav, A.; Yadav, R.; Mittal, A.; Wazir, N.H.; Gupta, S.; Pachauri, R.K.; Ghosh, S. A novel reconfiguration technique for improvement of PV reliability. *Renew. Energy* **2022**, *182*, 508–520. [[CrossRef](#)]
111. Krishna, G.S.; Moger, T. Improved SuDoKu reconfiguration technique for total-cross-tied PV array to enhance maximum power under partial shading conditions. *Renew. Sustain. Energy Rev.* **2019**, *109*, 333–348. [[CrossRef](#)]
112. Meerimatha, G.; Rao, L. Novel reconfiguration approach to reduce line losses of the photovoltaic array under various shading conditions. *Energy* **2020**, *196*, 117120. [[CrossRef](#)]
113. Calcabrini, A.; Muttillio, M.; Weegink, R.; Manganiello, P.; Zeman, M.; Isabella, O. A fully reconfigurable series-parallel photovoltaic module for higher energy yields in urban environments. *Renew. Energy* **2021**, *179*, 1–11. [[CrossRef](#)]
114. Malathy, S.; Ramaprabha, R. Reconfiguration strategies to extract maximum power from photovoltaic array under partially shaded conditions. *Renew. Sustain. Energy Rev.* **2018**, *81*, 2922–2934. [[CrossRef](#)]
115. Potnuru, S.R.; Pattabiraman, D.; Ganesan, S.I.; Chilakapati, N. Positioning of PV panels for reduction in line losses and mismatch losses in PV array. *Renew. Energy* **2015**, *78*, 264–275. [[CrossRef](#)]
116. Nihanth, M.S.S.; Ram, J.P.; Pillai, D.S.; Ghias, A.M.; Garg, A.; Rajasekar, N. Enhanced power production in PV arrays using a new skyscraper puzzle based one-time reconfiguration procedure under partial shade conditions (PSCs). *Sol. Energy* **2019**, *194*, 209–224. [[CrossRef](#)]
117. Osmani, K.; Haddad, A.; Lemenand, T.; Castanier, B.; Ramadan, M. An investigation on maximum power extraction algorithms from PV systems with corresponding DC-DC converters. *Energy* **2021**, *224*, 120092. [[CrossRef](#)]
118. Jaschke, R. Conduction Losses in DC/DC-Converters as buckboost/boostbuck synchronous rectifier types. In Proceedings of the 2007 Compatibility in Power Electronics, IEEE, Gdansk, Poland, 29 May–1 June 2007. [[CrossRef](#)]
119. Ayachit, A.; Kazimierzczuk, M.K. Averaged Small-Signal Model of PWM DC-DC Converters in CCM Including Switching Power Loss. *IEEE Trans. Circuits Syst. II Express Briefs* **2018**, *66*, 262–266. [[CrossRef](#)]
120. Panda, A.K.; Aroul, K. A Novel Technique to Reduce the Switching Losses in a Synchronous Buck Converter. In Proceedings of the 2006 International Conference on Power Electronic, Drives and Energy Systems, IEEE, New Delhi, India, 12–15 December 2006. [[CrossRef](#)]
121. Abu-aisheh, A.A.; Batarseh, M.G. *Chapter 15—DC-DC Converters. Electric Renewable Energy Systems*; Academic Press: Cambridge, MA, USA, 2016; pp. 337–353.
122. Available online: <https://www.onsemi.com/pub/Collateral/AND9135-D.PDF> (accessed on 1 April 2023).
123. Jadhav, S.; Devdas, N.; Nisar, S.; Bajpai, V. Bidirectional DC-DC converter in Solar PV System for Battery Charging Application. In Proceedings of the 2018 International Conference on Smart City and Emerging Technology (ICSCET), IEEE, Mumbai, India, 5 January 2018. [[CrossRef](#)]

Disclaimer/Publisher’s Note: The statements, opinions and data contained in all publications are solely those of the individual author(s) and contributor(s) and not of MDPI and/or the editor(s). MDPI and/or the editor(s) disclaim responsibility for any injury to people or property resulting from any ideas, methods, instructions or products referred to in the content.